Chapter - 3

Structural Characterization

3.1. Instrumentation

This chapter contain the fundamental details of the characterization techniques used to characterize the synthesized phosphor. It contains basic information about X-ray diffraction, Fourier Transform Infra-Red spectroscopy (FTIR) and Scanning Electron Microscopy (SEM). Chapter contains experimental results, discussion and its outcomes of above-mentioned characterization techniques of rare earth doped strontium pyrophosphate.

3.1.1. X-ray diffraction

3.1.1.1. Basic Information

The origin of the word 'crystallography' in the science and material technology was came from the study of macroscopic crystal forms. Hull (1919) pointed out that *"Every crystalline substance gives a pattern; the same substance always gives the same pattern; and in a mixture of substances each produces its pattern independently of the others*"[1, 2]. The first definition word 'crystal' has been given by Buerger (1956). He stated that *"a region of matter within which the atoms are arranged in a three-dimensional translationally periodic pattern"*[3]. With the help experimental and theoretical advent of the x-ray diffraction phenomenon, the science has been introduced to the study of atomic arrangements in crystalline materials. The systematic arrangement of atoms or molecules in a crystalline material is called as the crystal structure. In material science, majority of synthesized materials and some of the naturally abundant materials can be designated as crystalline material and x-ray diffraction (XRD) is one of the powerful technique used for the identification or the characterizing all such crystalline materials [4-6]. XRD provides the detail information of crystal structures, phases, preferred crystal orientations (texture), and other structural parameters, such as average grain size, crystallinity, strain, crystal defects, etc [7, 8]. Powder XRD is extensively used in various field such as geology, environmental science, material science, engineering, and biology for the identification of unknown crystalline materials like minerals, inorganic compounds [7, 9].

3.1.1.2. Principle

Powder x-ray diffraction pattern contains intense peaks produced due to the constructive interference of a monochromatic x-ray beam scattered at particular angles from each set of lattice planes formed in the material [10, 11]. These peak intensities in

the XRD pattern can resolute the distribution of atoms within the lattice and the spacing between the planes. The XRD pattern is the characteristic of periodic arrangement of the atoms in a material [6]. The peak intensities of XRD pattern depend on several factors such as structure parameter, incident intensity, slit width, operating voltage, and current used in the X-ray source [11].

3.1.1.3. Instrumentation used for x-ray diffraction

X-ray diffraction measurements of all synthesized samples has been done at UGC-CSR, Indore Center. XRD measurements were recorded through the Bruker D8 advance x-ray diffractometer shown in Figure 3.1. The diffractometer working on the basis of 1-D position sensitive detector based on silicon drift detector technique which reduces the measurement time significantly without reduction in the diffracted intensity. Cu-Kα is used as x-ray source in Bruker D8 Advance diffractometer. The wavelength of generated x-ray is 0.15406 nm for operating voltage 40 kV and current 40 mA. The XRD measurements were carried out for glancing angle incidence detector at an angle of 2° for 2θ values of 10°–60° in steps of 0.02° s^{-1}.

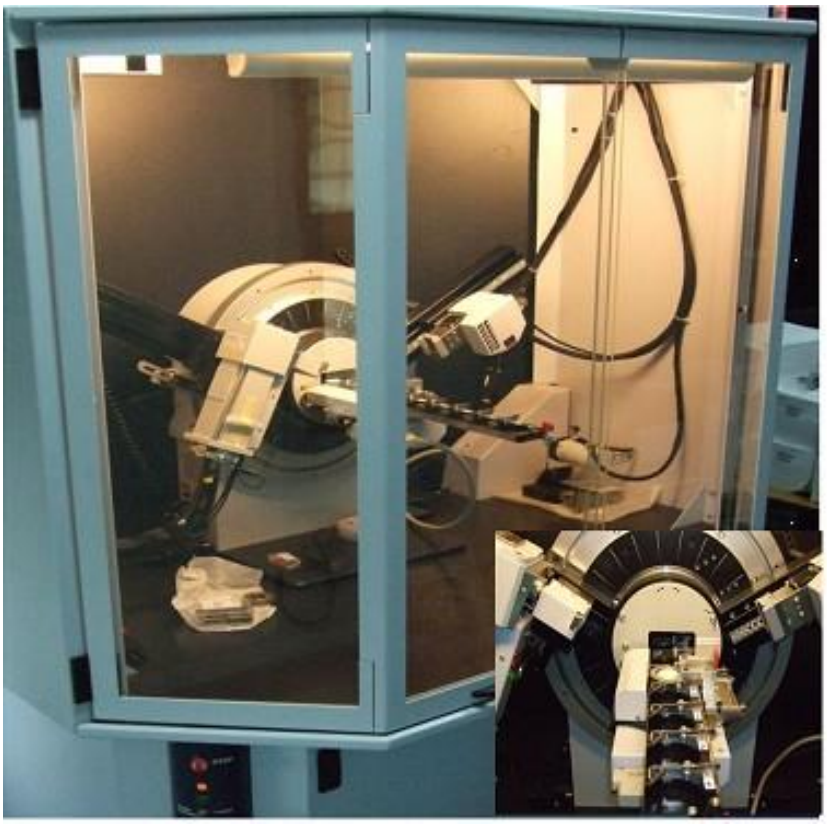

Figure 3.1 Bruker D8 advance x-ray diffractometer.

3.1.1.4. Uses of XRD

Listed of uses of the powder x-ray diffraction are in various branch of science are given below.

XRD is well-known technique for identify the single-phase materials like minerals, chemical compounds, ceramics or other engineered materials as well as to identify the multiple phases in microcrystalline mixtures (i.e., rocks). It is used for the determination of the crystal structure of identified materials. It is used for identify the percentage amount of amorphous materials in partially crystalline mixtures. The structural analysis and calculations of unit-cell for crystalline materials can also done by XRD. It is used for quantitative determination of amounts of different phases in multi-phase mixtures by peak-ratio calculations, quantitative determination of phases by whole-pattern refinement. It is used for determination of crystallite size from analysis of peak broadening, determine of crystallite shape from study of peak symmetry in XRD pattern.

3.1.2. Fourier Transform Infrared Spectroscopy

3.1.2.1. Basic Information

FTIR spectroscopy is a most powerful characterization method for the identification of functional groups present in the materials for both organic and inorganic materials at a variety of levels [12, 13]. The mid-infrared spectrum of the wavelength range approximately 4000 – 400 cm^{-1} is used in IR spectroscopy for identification of the fundamental rotational-vibrational modes in the material structure. The fingerprint region (600 -1500 cm^{-1}) of IR spectrum is the most important regions which cannot used easily to identify unknown specimen in the material [14, 15]. FTIR can be used to recognize some components present inside the unknown mixture and for the analysis of solids, liquids, and gases. FTIR spectroscopy is the study of behavior of molecules during the interaction of matter with the light radiation when IR waves travel through the matter [16]. The IR waves interact with the polar molecules of the chemical bonds, if there is no polarity or dipole moment in the molecule then IR interaction becomes insensitive as a result the molecules does not produce any IR spectrum [17].

3.1.2.2. Principle

Absorption of IR region of electromagnetic radiation spectrum by the molecules that promotes the transitions between the rotational and vibrational energy levels of the ground state [15, 18]. IR spectroscopy is concerned primarily with molecular

vibrations, as transitions between individual rotational states can be measured only in the infrared spectra of small molecules in the gas phase [19-21]. Molecular bonds can vibrate at different frequencies depending upon the type of elements and the type of bonds formed in material, for a bond, have several specific frequencies due the verity of vibration [22, 23]. According to quantum mechanics, these vibrational frequencies of molecules correspond to the ground state and excited states are originated due to the excitation of the bond by absorption of light energy [24]. The absorbed light energy for a transition must equivalent to that of the energy difference between the ground state and excited state. Fourier Transform Infrared (FTIR) Spectroscopy is referred to the development of the data processing in the manner, in which the data is collected and converted from an interference pattern to a spectrum [25, 26].

3.1.2.3. Instrument Used for FTIR

FTIR measurements of all synthesized samples has been done at Department of Physics, The M. S. University of Baroda, Vadodara. FTIR spectra were recorded through the JASCO – 4600 Fourier Transform Infra-Red spectrometer shown in Figure 3.2. Fourier transform infrared (FTIR) spectra of the samples were recorded by FTIR-4100 type A IR spectrometer in transmittance mode in wavenumber range of 400–4000 cm^{-1}.

Figure 3.2 JASCO – 4600 Fourier Transform Infra-Red spectrometer**.**

3.1.2.4. Uses of FTIR

Listed of uses of the powder FTIR spectroscopy are in various branch of science are given below.

IR spectroscopy can provide information of isolated materials, biomaterials, such as biopolymers as well as biological materials, connective tissues, single cells and in general biological fluids to give only a few examples [15, 27]. Infrared spectroscopy could be used to analyze almost all organic compounds and some inorganic compounds. It has a wide range of application in both qualitative analysis and quantitative analysis. Also, the sample of Infrared spectroscopy doesn't have phase constraints. It could be gas, liquid or solid, which has enlarged the range of analysts.

3.1.3. Scanning Electron Microscopy (SEM)

3.1.3.1. Basis Information

The discovery of electron microscopes is occurred due to the limitations of light microscopes. Light microscopes have limitation to magnify the objects up to the range of visible light [28, 29]. As the dimensions of the particle size of material science and other scientific exercises are reduced up to the order of micro to nano size, it cannot possible to analyze of characterized the structures by light microscopy. Scanning Electron Microscope (SEM) is an instrument that can use high energy electron beam to scan an object on a very fine scale of the order of micro to nanoscale [30]. The scanning of object can produce information about the topography, morphology, composition and crystallographic information the object, and other properties such as electrical conductivity. SEM is used primarily to examine the surfaces of objects [31].

3.1.3.2. Principle

In SEM, high energy electron beam incident on the material that can produce secondary electron according to the structure and morphology of the material [30, 32]. These secondary electron are collected by the positively charged detector placed at high potential. The detected secondary electrons produce scintillations effect on to the photomultiplier tube which can convert into electrical signals. The produced signals are further amplified by the video amplifier and system convert it into 3- dimensional image of the sample. In SEM, the image formed due to the interaction of the incident electron with the material that produce various signals, which can be used to obtain information about the surface topography and composition [31, 33].

3.1.3.3. Instrument Used for SEM

SEM measurements of all synthesized samples has been done at. SEM images were recorded through the "JSM-7500F" field emission scanning electron microscope (SEM) shown in Figure 3.3. The "JSM-7500F" field emission scanning electron microscope (SEM) has features of an optical system that includes a semi-in-lens type objective lens, which can use to collimate the electron beam even at low accelerating voltages. The general purpose of JSM-7500F SEM system is deliver high-resolution image of the specimens.

Figure 3.3 "JSM-7500F" field emission scanning electron microscope (SEM).

3.1.3.4. Uses of SEM

SEM have wide range of application in fields of various branch of science and engineering that allowing researchers working on a wide range of projects in the different fields to access useful information about microscopic processes take place in their research with macroscopic inferences. SEM is widely used to examine the surface topographies of the object or materials, morphology of the materials like shape and size of the particles, composition of the materials like the different elements and compounds that the object contain and the relative percentage of amounts of elements, crystallographic information such as structure of particle (nanoscience) and porosity of the material, etc.

3.2. Structural Characterization

3.2.1. X-ray Diffraction

3.2.1.1. $Sr_2P_2O_7$: RE (RE = Ce^{3+}, Eu^{3+}, Tb^{3+}, Dy^{3+}, Er^{3+}, Gd^{3+})

XRD patterns of pure $Sr_2P_2O_7$ and JCPDS: 24-1011 are shown in Figure 3.4. The XRD patterns of $Sr_2P_2O_7$: x RE (x = 0.5, 1.0, 1.5, 2.0, 2.5 and 5.0 mol%; RE = Ce^{3+}, Eu^{3+}, Tb^{3+}, Dy^{3+}, Er^{3+} and Gd^{3+}) are shown in Figure 3.6(A) – 3.11 (A). The XRD patterns of rare earth doped $Sr_2P_2O_7$ samples are compared with JCPDS standard card no. 24-1011. The hkl parameters of the prepared samples are similar to that of the JCPDS standard card no. 24-1011 of α-$Sr_2P_2O_7$ that indicates the existence of a pure single-phase α-$Sr_2P_2O_7$. The structural parameters of the samples were analyzed using powder software for XRD analysis. The analysis confirms that the samples have a pure α-phase with crystallization in the orthorhombic structure and space group of P_{nam}. The doping of various rare earth ions and their percentage concentration does not make any perceptible variation in XRD patterns as well as no other peaks found than that of $Sr_2P_2O_7$ in these patterns. This indicates that the prepared samples are single phased and substitution of Sr^{2+} by RE^{3+} does not cause any substantial modification in the crystal structure of host. Some prominent intense peaks are observed in the XRD patterns at different 2θ values of 12.12°, 25.95°, 26.27°, 26.93°, 33.16°, 33.63° and 44.40° corresponding to the (110), (201), (031), (211), (002), (141) and (232) planes for these host lattice respectively. Sharp intense peaks in the XRD patterns of all rare earth doped samples signify that all samples are polycrystalline material. Detailed lattice parameters of pure $Sr_2P_2O_7$ calculated from the experimental data using powderX software and the values reported in literature are summarized in Table 3.1. The calculated crystalline parameters of RE^{3+} doped $Sr_2P_2O_7$ phosphors are summarized in Table 3.2 – 3.7. The analyzed XRD pattern of pure $Sr_2P_2O_7$ is shown in Figure 3.5.

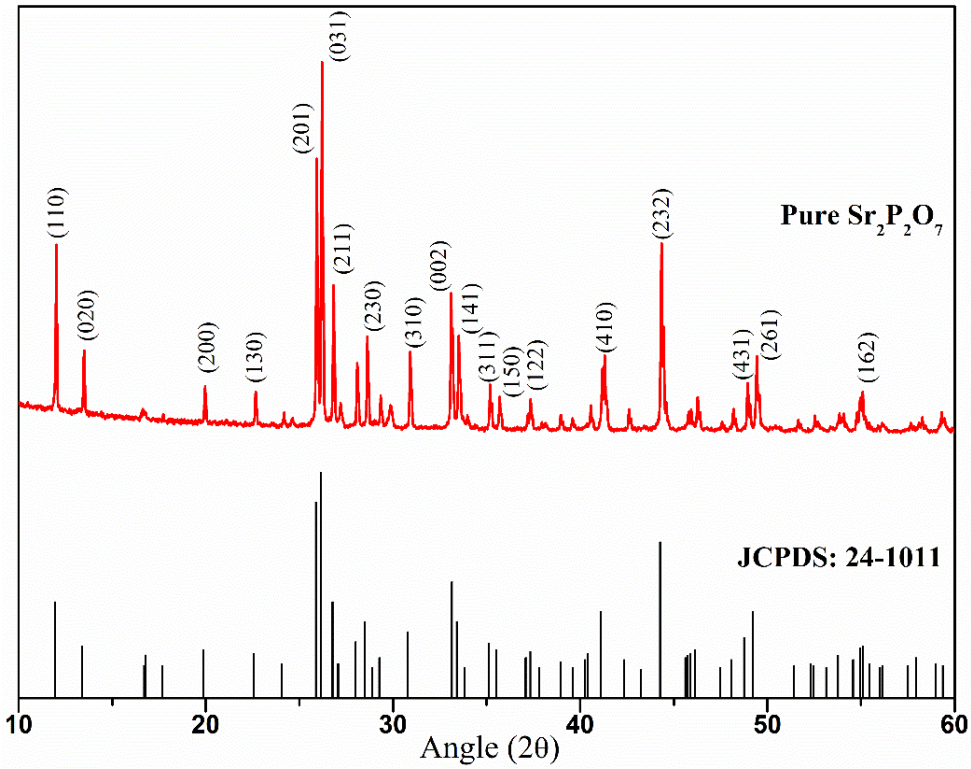

Figure 3.4 XRD patterns of pure $Sr_2P_2O_7$ and JCPDS: 24-1011.

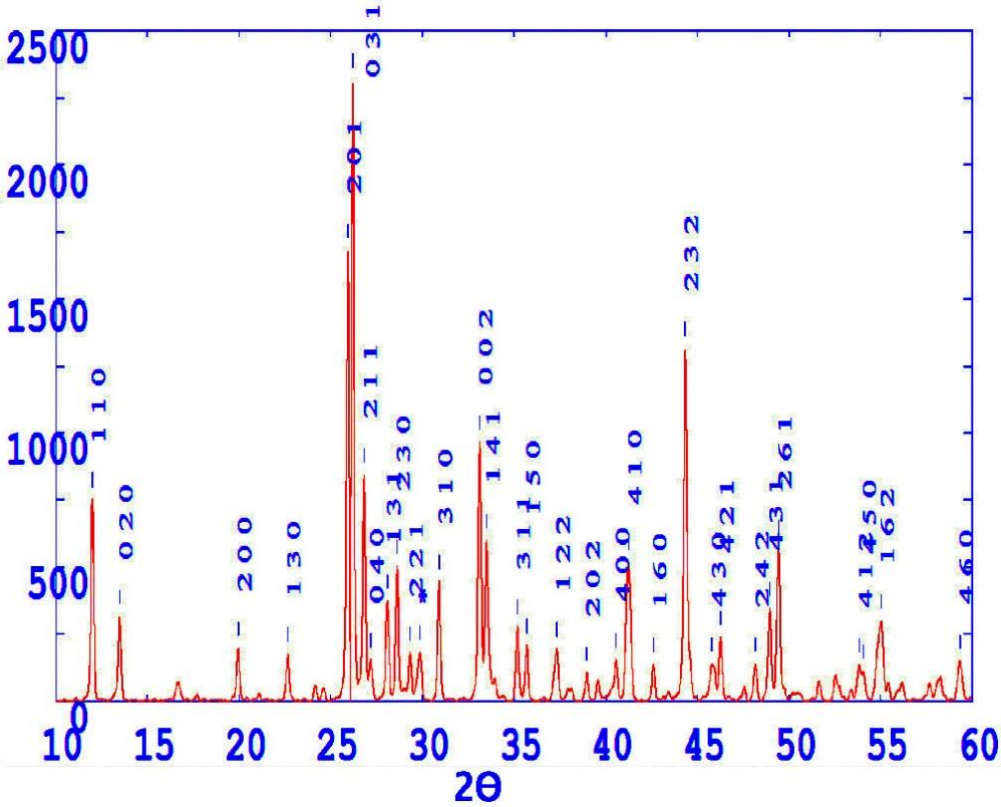

Figure 3.5 XRD patterns of $Sr_2P_2O_7$ analyzed using powderX software.

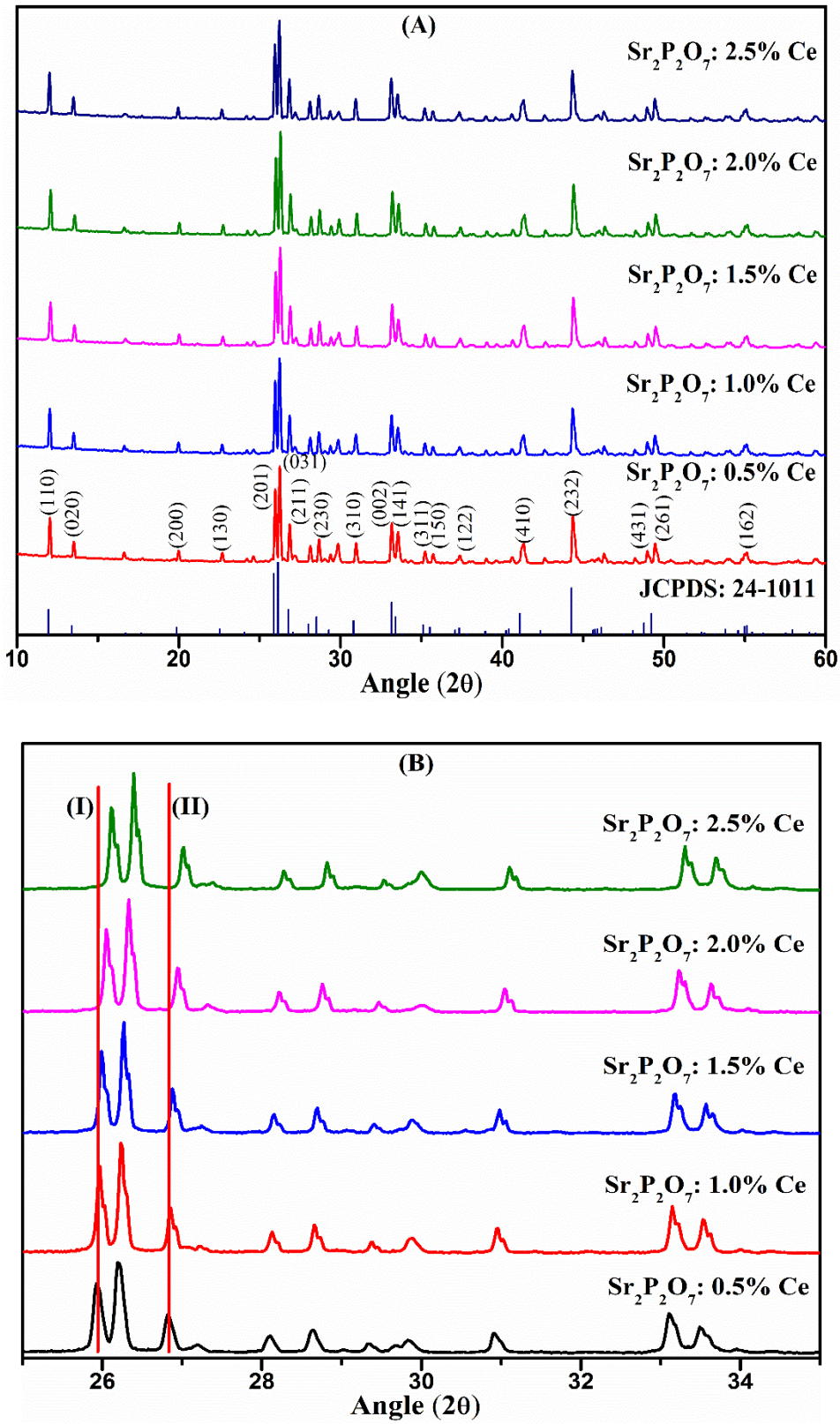

Figure 3.6 (A) XRD patterns of $Sr_2P_2O_7$: x Ce^{3+} (x = 0.5, 1.0, 1.5, 2.0 and 2.5 mol%) phosphor and JCPDs Card No. 24-1011. (B) Magnified XRD patterns.

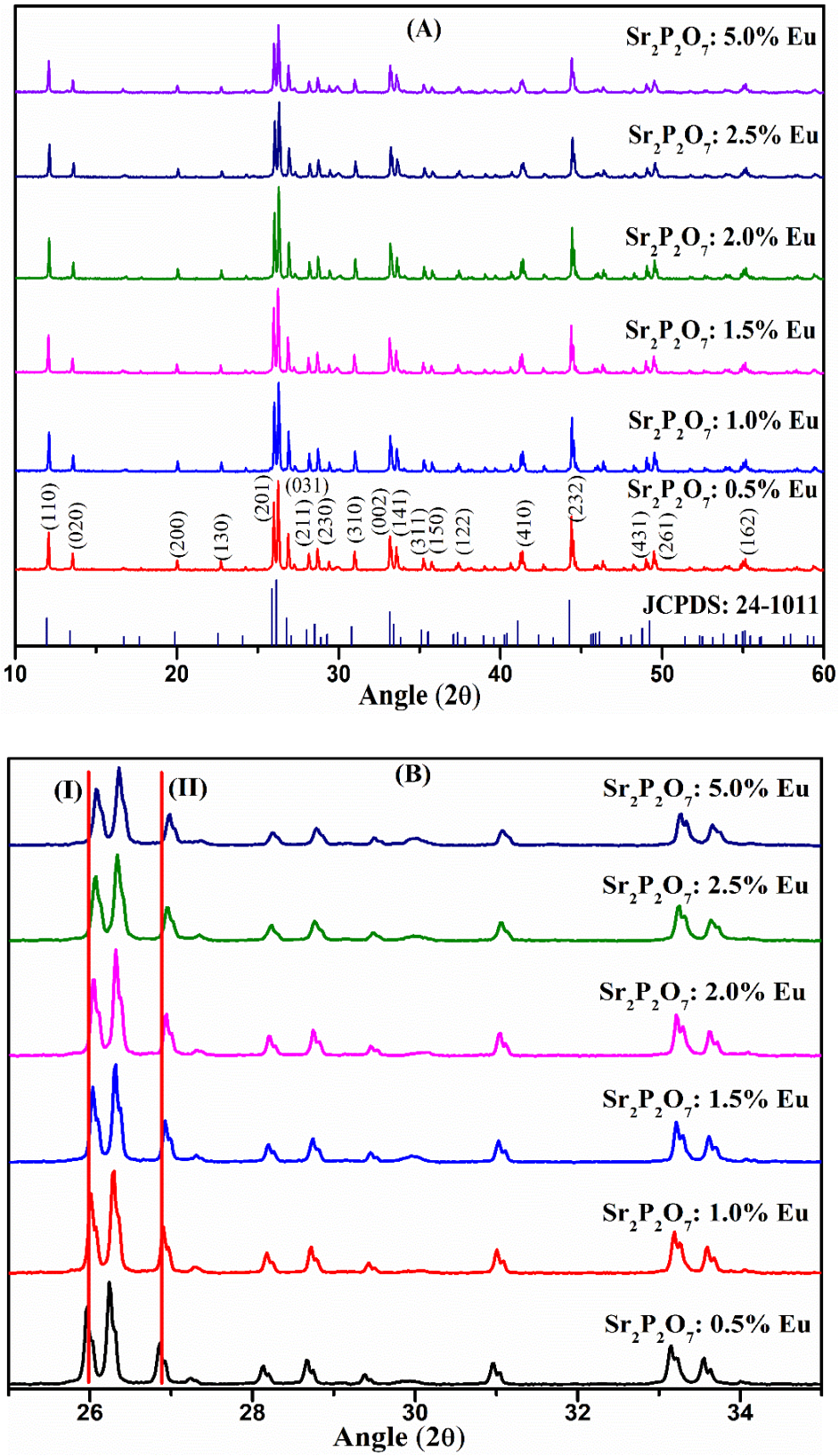

Figure 3.7 (A) XRD patterns of $Sr_2P_2O_7$: x Eu^{3+} (x = 0.5, 1.0, 1.5, 2.0, 2.5 and 5.0 mol%) phosphor and JCPDs Card No. 24-1011. (B) Magnified XRD patterns.

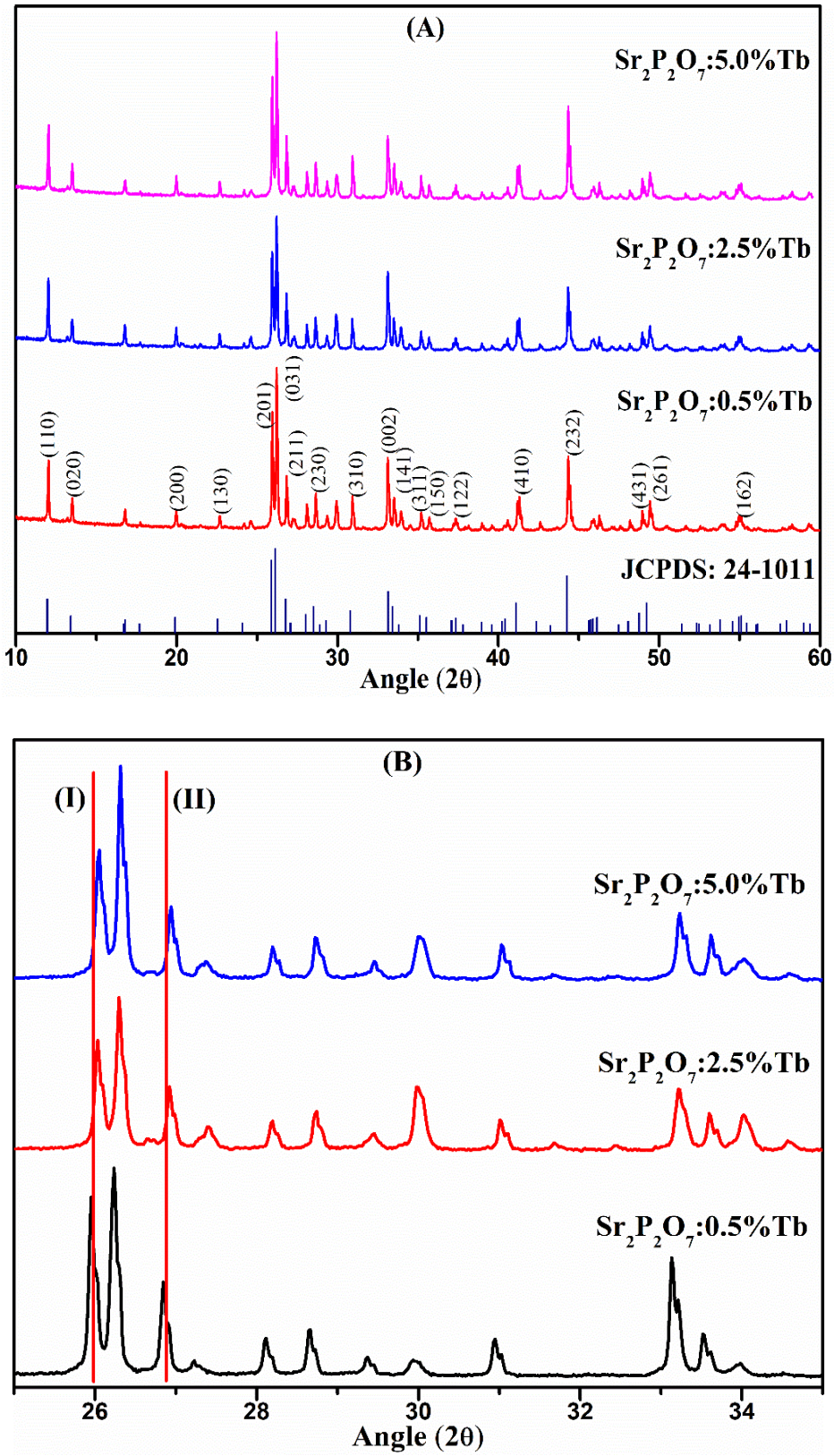

Figure 3.8 (A) XRD patterns of $Sr_2P_2O_7$: x Tb^{3+} (x = 0.5, 2.5 and 5.0 mol%) phosphor and JCPDs Card No. 24-1011. (B) Magnified XRD patterns.

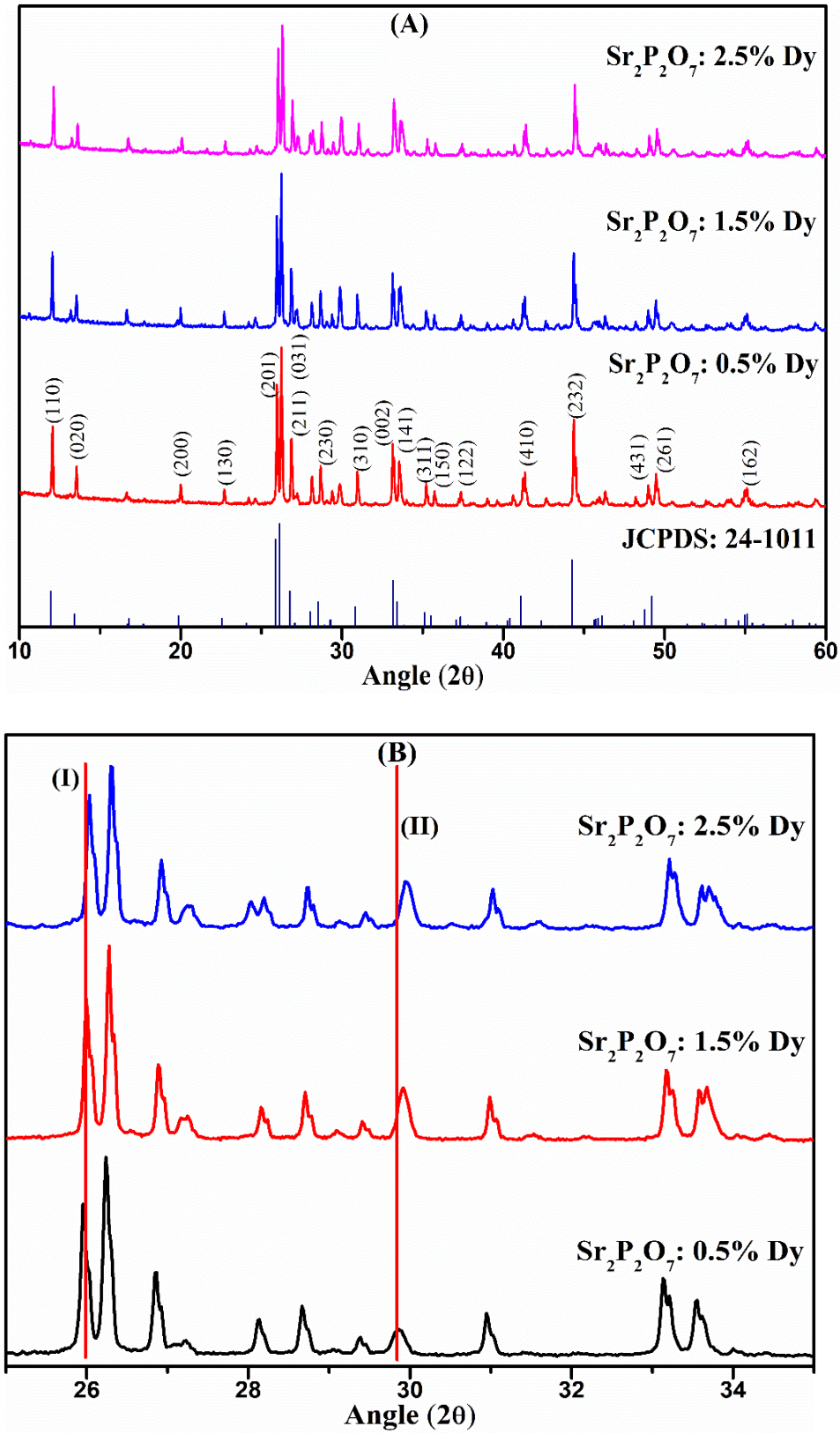

Figure 3.9 (A) XRD patterns of $Sr_2P_2O_7$: x Dy^{3+} (x = 0.5, 1.5 and 2.5 mol%) phosphor and JCPDs Card No. 24-1011. (B) Magnified XRD patterns.

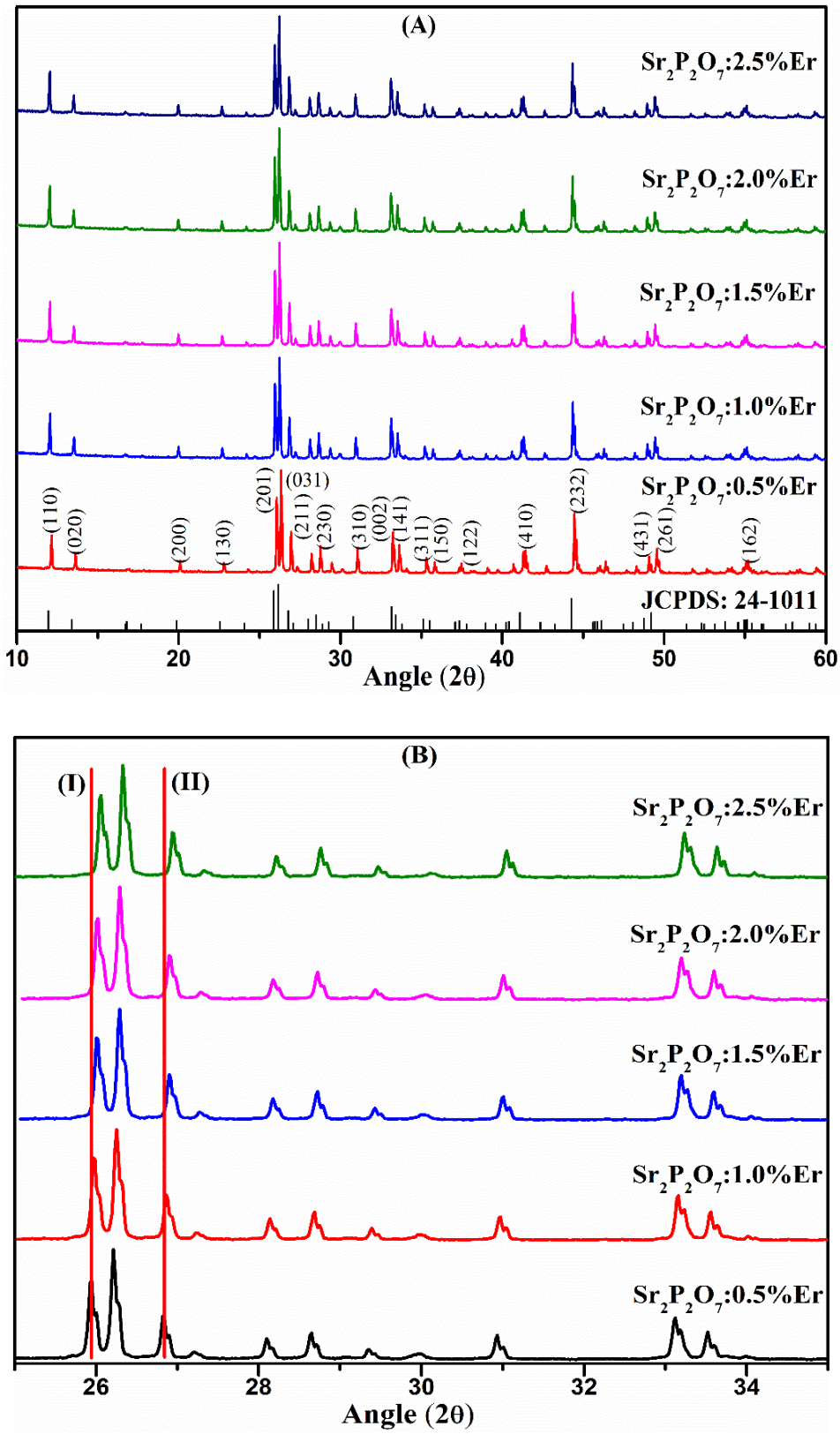

Figure 3.10 (A) XRD patterns of $Sr_2P_2O_7$: x Er^{3+} (x = 0.5, 1.0, 1.5, 2.0 and 2.5 mol%) phosphor and JCPDs Card No. 24-1011. (B) Magnified XRD patterns.

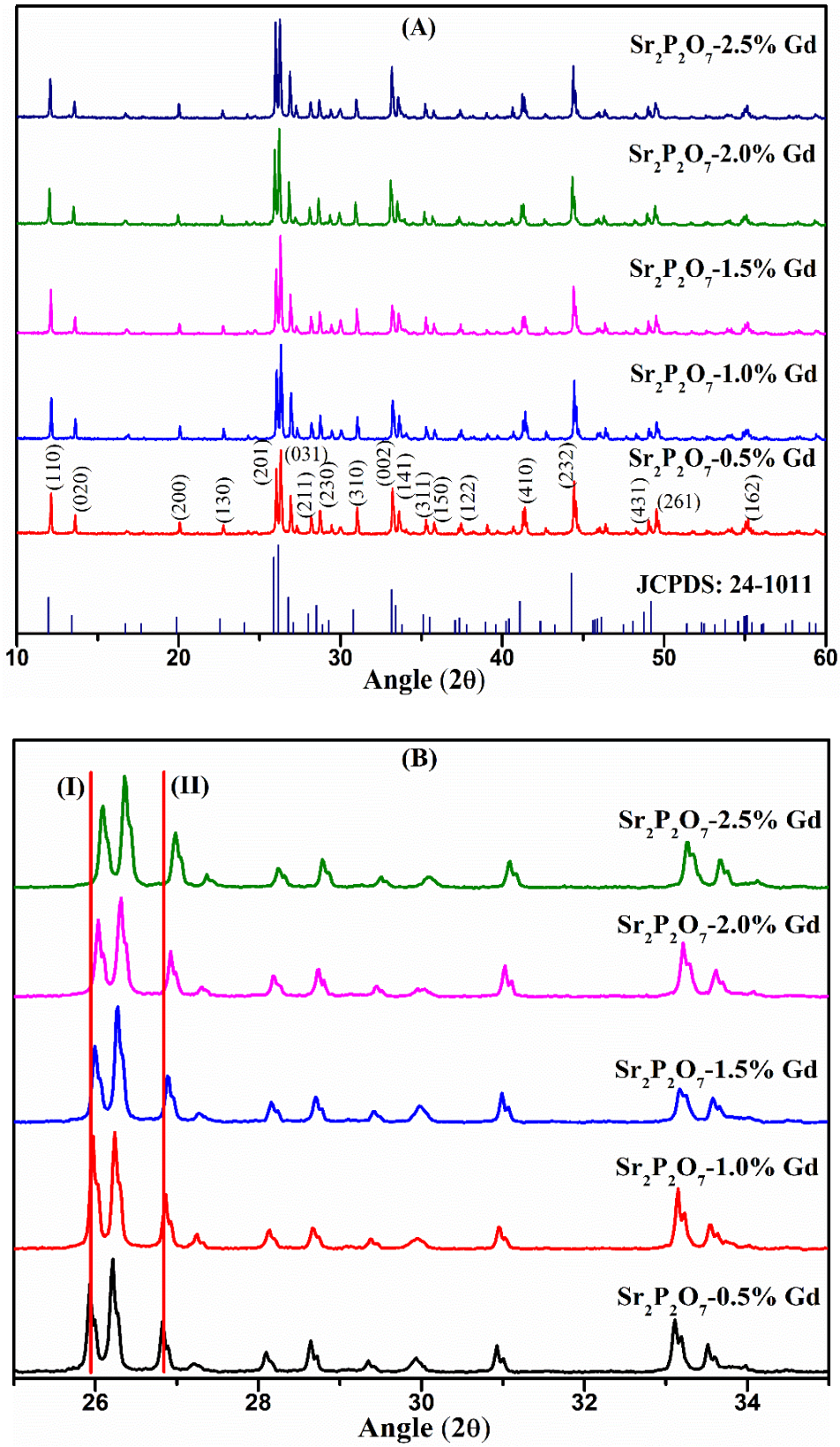

Figure 3.11 (A) XRD patterns of $Sr_2P_2O_7$: x Gd^{3+} (x = 0.5, 1.0, 1.5, 2.0 and 2.5 mol%) phosphor and JCPDs Card No. 24-1011. (B) Magnified XRD patterns.

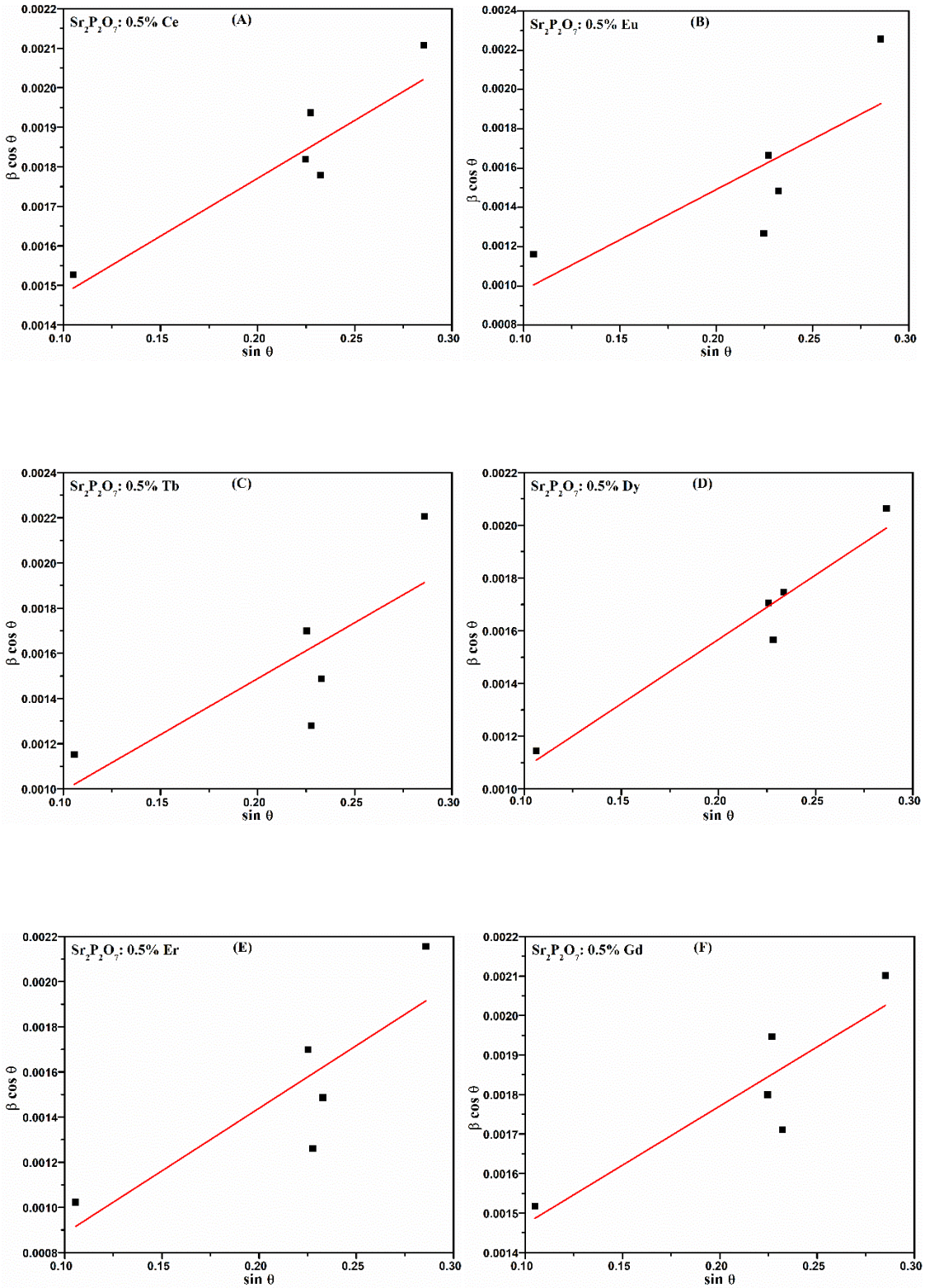

Figure 3.12 Williamson-Hall plot: (A) $Sr_2P_2O_7$: 0.5% Ce^{3+}; (B) $Sr_2P_2O_7$: 0.5% Eu^{3+}; (C) $Sr_2P_2O_7$: 0.5% Tb^{3+}; (D) $Sr_2P_2O_7$: 0.5% Dy^{3+}; (E) $Sr_2P_2O_7$: 0.5% Er^{3+}; (E) $Sr_2P_2O_7$: 0.5% Gd^{3+}phosphor.

JCPDS (24-1011) Data					Experimental Data $Sr_2P_2O_7$				
a = 8.917 Å	b = 13.160 Å		c = 5.400 Å		a = 8.993 Å	b = 13.236 Å		c = 5.523 Å	
V = 633.677 Å^3					V = 657.648 Å^3				
2θ	d	h	k	l	$2\theta_{Exp}$	d_{Exp}	h	k	l
11.950	7.400	1	1	0	12.016	7.36	1	1	0
13.404	6.600	0	2	0	13.512	6.548	0	2	0
19.882	4.462	2	0	0	19.962	4.444	2	0	0
22.548	3.940	1	3	0	22.672	3.919	1	3	0
25.886	3.439	2	0	1	25.927	3.434	2	0	1
26.141	3.406	0	3	1	26.210	3.397	0	3	1
26.774	3.327	2	1	1	26.817	3.322	2	1	1
28.018	3.182	1	3	1	28.091	3.173	1	3	1
28.512	3.128	2	3	0	28.636	3.115	2	3	0
30.807	2.900	3	1	0	30.921	2.890	3	1	0
33.152	2.700	0	0	2	33.105	2.704	0	0	2
33.407	2.680	1	4	1	33.509	2.672	1	4	1
35.107	2.554	3	1	1	35.188	2.549	3	1	1
35.524	2.525	1	5	0	35.693	2.514	1	5	0
37.344	2.406	1	2	2	37.351	2.406	1	2	2
44.277	2.044	2	3	2	44.347	2.041	2	3	2
46.133	1.966	4	2	1	46.288	1.960	4	2	1
48.761	1.866	4	3	1	48.957	1.859	4	3	1
49.211	1.850	2	6	1	49.443	1.842	2	6	1
55.114	1.665	0	3	3	55.104	1.665	0	3	3

Table 3.1 Comparison of experimental XRD data of $Sr_2P_2O_7$ with published JCPDS 24-1011 data.

Sample	Lattice Parameter			Volume of Unit Cell 'V' (Å ^{3})
	a (Å)	b (Å)	c (Å)	
$Sr_2P_2O_7$: 0.5 mol% Ce^{3+}	8.984	13.193	5.451	646.08
$Sr_2P_2O_7$: 1.0 mol% Ce^{3+}	8.976	13.185	5.447	644.64
$Sr_2P_2O_7$: 1.5 mol% Ce^{3+}	8.865	13.176	5.441	635.53
$Sr_2P_2O_7$: 2.0 mol% Ce^{3+}	8.861	13.167	5.437	634.34
$Sr_2P_2O_7$: 2.5 mol% Ce^{3+}	8.854	13.156	5.431	632.62

Table 3.2 Crystal structure parameters of $Sr_2P_2O_7$: x Ce^{3+} (x = 0.1, 0.5, 1.0, 1.5, 2.0 and 2.5 mol%).

Sample	Lattice Parameter			Volume of Unit Cell 'V' (Å ^{3})
	a (Å)	b (Å)	c (Å)	
$Sr_2P_2O_7$: 0.5 mol% Eu^{3+}	8.872	13.175	5.442	636.11
$Sr_2P_2O_7$: 1.0 mol% Eu^{3+}	8.867	13.168	5.435	634.59
$Sr_2P_2O_7$: 1.5 mol% Eu^{3+}	8.861	13.160	5.429	633.08
$Sr_2P_2O_7$: 2.0 mol% Eu^{3+}	8.852	13.155	5.422	631.38
$Sr_2P_2O_7$: 2.5 mol% Eu^{3+}	8.847	13.146	5.417	630.01
$Sr_2P_2O_7$: 5.0 mol% Eu^{3+}	8.829	13.121	5.397	625.21

Table 3.3 Crystal structure parameters $Sr_2P_2O_7$: x Eu^{3+} (x = 0.5, 1.0, 1.5, 2.0, 2.5 and 5.0 mol%).

Sample	Lattice Parameter			Volume of Unit Cell 'V' (Å ^{3})
	a (Å)	b (Å)	c (Å)	
$Sr_2P_2O_7$: 0.5 mol% Tb^{3+}	8.857	13.145	5.434	632.65
$Sr_2P_2O_7$: 2.5 mol% Tb^{3+}	8.832	13.123	5.415	627.61
$Sr_2P_2O_7$: 5.0 mol% Tb^{3+}	8.817	13.105	5.387	622.45

Table 3.4 Crystal structure parameters of $Sr_2P_2O_7$: x Tb^{3+} (x = 0.5, 2.5 and 5.0 mol%).

Sample	Lattice Parameter			Volume of Unit Cell 'V' (Å ^{3})
	a (Å)	b (Å)	c (Å)	
$Sr_2P_2O_7$: 0.5 mol% Dy^{3+}	8.851	13.132	5.427	630.78
$Sr_2P_2O_7$: 1.5 mol% Dy^{3+}	8.842	13.126	5.419	628.93
$Sr_2P_2O_7$: 2.5 mol% Dy^{3+}	8.829	13.113	5.406	625.88

Table 3.5 Crystal structure parameters of $Sr_2P_2O_7$: xDy^{3+} (x = 0.5, 1.5 and 2.5 mol%).

Sample	Lattice Parameter			Volume of Unit Cell 'V' (Å ^{3})
	a (Å)	b (Å)	c (Å)	
$Sr_2P_2O_7$: 0.5 mol% Er^{3+}	8.837	13.117	5.408	626.87
$Sr_2P_2O_7$: 1.0 mol% Er^{3+}	8.831	13.111	5.401	625.34
$Sr_2P_2O_7$: 1.5 mol% Er^{3+}	8.823	13.104	5.397	623.98
$Sr_2P_2O_7$: 2.0 mol% Er^{3+}	8.814	13.095	5.389	621.99
$Sr_2P_2O_7$: 2.5 mol% Er^{3+}	8.808	13.089	5.380	620.25

Table 3.6 Crystal structure parameters of $Sr_2P_2O_7$: x Er^{3+} (x = 0.5, 1.0, 1.5, 2.0 and 2.5 mol%).

Sample	Lattice Parameter			Volume of Unit Cell 'V' (Å ^{3})
	a (Å)	b (Å)	c (Å)	
$Sr_2P_2O_7$: 0.5 mol% Gd^{3+}	8.867	13.162	5.431	633.84
$Sr_2P_2O_7$: 1.0 mol% Gd^{3+}	8.858	13.157	5.425	632.25
$Sr_2P_2O_7$: 1.5 mol% Gd^{3+}	8.850	13.153	5.418	630.67
$Sr_2P_2O_7$: 2.0 mol% Gd^{3+}	8.846	13.147	5.411	629.29
$Sr_2P_2O_7$: 2.5 mol% Gd^{3+}	8.840	13.141	5.405	627.88

Table 3.7 Crystal structure parameters of $Sr_2P_2O_7$: x Gd^{3+} (x = 0.5, 1.0, 1.5, 2.0 and 2.5 mol%).

Samples →	$Sr_2P_2O_7$: Ce^{3+}	$Sr_2P_2O_7$: Eu^{3+}	$Sr_2P_2O_7$: Tb^{3+}	$Sr_2P_2O_7$: Dy^{3+}	$Sr_2P_2O_7$: Er^{3+}	$Sr_2P_2O_7$: Gd^{3+}
Doping Concentration ↓	**Crystallite Size (nm)**					
0.5 mol%	82.55	72.83	69.46	68.29	61.54	71.53
1.0 mol%	81.40	71.97	----	----	60.13	70.17
1.5 mol%	79.21	70.47	----	66.69	58.84	69.99
2.0 mol%	78.19	68.93	----	----	57.35	67.82
2.5 mol%	77.54	68.04	65.79	63.53	55.87	66.38
5.0 mol%	----	65.89	63.65	----	----	----

Table 3.8 Crystallite Size of $Sr_2P_2O_7$: RE (RE = Ce^{3+}, Eu^{3+}, Tb^{3+}, Dy^{3+}, Er^{3+} Gd^{3+}) calculated through Scherrer's formula.

Samples →	$Sr_2P_2O_7$: Ce^{3+}	$Sr_2P_2O_7$: Eu^{3+}	$Sr_2P_2O_7$: Tb^{3+}	$Sr_2P_2O_7$: Dy^{3+}	$Sr_2P_2O_7$: Er^{3+}	$Sr_2P_2O_7$: Gd^{3+}
Doping Concentration ↓	**Crystallite Size (nm)**					
0.5 mol%	88.62	79.32	78.67	81.38	72.37	85.33
1.0 mol%	86.78	76.93	----	----	69.59	82.27
1.5 mol%	85.11	74.87	----	76.90	68.25	79.19
2.0 mol%	83.43	71.82	----	----	64.95	74.62
2.5 mol%	80.76	70.14	70.58	71.47	61.53	72.43
5.0 mol%	----	68.92	67.54	----	----	----

Table 3.9 Crystallite Size of $Sr_2P_2O_7$: RE (RE = Ce^{3+}, Eu^{3+}, Tb^{3+}, Dy^{3+}, Er^{3+} Gd^{3+}) calculated trough Williamson-Hall plot analysis.

$Sr_2P_2O_7$ displays two types of polymorphic form, a low-temperature β-phase with a tetragonal structure, and a high-temperature α-phase with an orthorhombic structure [34]. The diffraction peaks of a powder XRD pattern of $Sr_2P_2O_7$ are very sharp because of high crystallinity. The average crystallite size of rare earth doped $Sr_2P_2O_7$ phosphors were calculated by using the Scherrer's formula given below [35]:

$$D = \frac{K\lambda}{\beta \cdot cos\theta}$$

Where D is the average crystallite size or ordered domain (in nm), λ is x-ray wavelength (λ= 1.54178 Å), β s the full-width half maximum (FWHM) of the intense

peaks of host lattice, and K is the shape factor (K = 0.9). In the Scherrer's formula, the FWHM values has been taken from the XRD analysis powderX data. The crystallite size of all phosphors were calculated from the most intense peaks having hkl values (201) and (031) in XRD pattern. The obtained results signify that as the doping concentration increases the volume of the unit cell and the crystallite size of the phosphor is decrease. The XRD patterns signify that the doping of RE^{3+} ion occupy the Sr^{2+} sites in $Sr_2P_2O_7$ lattice and its occupancy does not deform the basic pyrophosphate arrangement and there is no other impurity phase arise in host structure due to the impurity ions. The crystallite size of RE^{3+} doped $Sr_2P_2O_7$ calculated through Scherrer's formula are depicted in Table 3.8.

Williamson-Hall (W–H) plot analysis is a simple integral breath method to determine the crystallite size and strain prompted in material which can be results into the deformation XRD peak. In the W–H relation given for the crystallite size and strain, it is expected that the strain produced in the material is identical all the way through the crystallographic direction, which is given by β_{hkl} [36],

$$\beta_{hkl} = \frac{K\lambda}{D\ cos\theta} + 4\varepsilon\ tan\theta$$

$$\beta_{hkl}\ cos\theta = \frac{K\lambda}{D} + 4\varepsilon\ sin\theta$$

Where D is the crystallite size and ε is the microstrain. The graph of β cosθ vs sin θ be the straight line, the average crystallite size and the strain can be calculated by the Y-intercept extrapolation and the slope of the line shown in Figure 3.12. The formula for the crystallite size is given below,

$$D = \frac{K\lambda}{Y - Intercept}$$

The W-H plot of 0.5% RE^{3+} doped $Sr_2P_2O_7$ is shown in Figure 3.12. The crystallite size of RE^{3+} doped $Sr_2P_2O_7$ calculated through Williamson-Hall (W–H) plot analysis are depicted in Table 3.9. The crystallite size measured by two different method having nearer values for all synthesized phosphor. The magnified XRD pattern for 2θ range 25°-35° is shown in Figure 3.6(B) – 3.11(B). It is noted that there is minute shifting in peak position towards higher diffraction angle 2θ for the increment of doping concentration that can identify from the vertical lines (I) and (II) in Figure 3.6 – 3.11 (B), but there is no change in formation XRD patterns. The peak shifting towards higher 2θ value is observed in XRD pattern due to the increase in the doping

concentrations revealed that the more number of substitution of doping occurs at the place of Sr^{2+} site in host lattice. The shifting in peak position ensues due to decrease in unit cell size which can results due to the ionic radii difference of host ion Sr^{2+} and rare earth ion RE^{3+}. The percentage difference of Sr^{2+} ion and RE^{3+} ions summarized in Table 3.10. It is an evidence that the values of calculated radii percentage difference signify that the doping ion RE^{3+} successfully substitute the host ion Sr^{2+} in the host material $Sr_2P_2O_7$.

	RE Ions	**Ionic Radius 'IR' (Å)**	**R_{pd}**	**Z/IR**
Doped Ion	Ce^{3+}(9)	1.196	8.70	2.51
	Eu^{3+}(9)	1.120	14.50	2.68
	Tb^{3+}(9)	1.095	16.41	2.74
	Dy^{3+}(9)	1.083	17.33	2.77
	Er^{3+}(9)	1.062	18.93	2.822
	Gd^{3+}(9)	1.107	15.49	2.71
	Sm^{3+}(9)	1.132	13.59	2.65
	Nd^{3+}(9)	1.163	11.22	2.58
Substituted Ion	Sr^{2+}(9)	1.310		1.53

Table 3.10 Percentage difference of radius, and valance charge to ionic radius ratio of ions in phosphor [37, 38].

The percentage difference in the ion radii between doped ion and substituted ion is calculated by equation given below,

$$R_{pd} = 100\% \times \frac{R_{Sr^{2+}}(9) - R_{RE^{3+}}(9)}{R_{Sr^{2+}}(9)}$$

Where R_{pd} is the radius percentage difference, $R_{Sr^{2+}}(9)$ is the radius of the host cation with its defined coordination number, and $R_{RE^{3+}}(9)$ is the radius of doped rare-earth ions with its defined coordination number to occupy the lattice site of host ion. The appropriate substitution of the doping ion can take place if the radius percentage difference between the ionic radius of doped ion and substituted ion must not be more than 30% [39, 40]. The valance charge to ionic radius ratio (Z/IR) for doped ion and host cation is also determined which is mentioned with the radius percentage difference in Table 3.10. The small discrepancy of Z/IR ratio of doped and substituted ion reveals

that the easy occurrence of substitution of doped ion. Inside the crystal structure of $Sr_2P_2O_7$, Sr^{2+} ions occupy two different crystallographic sites where each Sr^{2+} ion had been coordinated by nine O^{2-} ions belonging to five different pyrophosphate groups [41]. In both lattice sites, Sr^{2+} ion is sitting at the center of the crystal structure of a quite similar SrO_9 polyhedron. The formed polyhedra can be originated from a cube where six oxygen atoms are close to six corners of the cube and remaining three O^{2-} are approximately arranged along the fourth parallel cube edge [42]. Inside the structure of $Sr_2P_2O_7$, both Sr^{2+} ion sites having centrosymmetry which could be a significant influence on the luminescence properties of the phosphor. This two types of centrosymmetric Sr^{2+} sites are coordinated by nine oxygen with average bond lengths of 2.721 Å and 2.679 Å for Sr_1 – O and for Sr_2 – O respectively [18,19]. In orthorhombic structure of strontium pyrophosphate t,wo types of PO_4 tetrahedrons groups are linked to each other by corner sharing and the Sr^{2+} ion has been isolated the P_2O_7, pyrophosphate groups. The average bond lengths of P_1 – O and P_2 – O of different corner phosphate groups are 1.541 and 1.542 Å respectively [43].

3.2.1.2. $Sr_2P_2O_7$: Ce^{3+}, RE (RE = Eu^{3+}, Tb^{3+}, Dy^{3+}, Er^{3+}, Gd^{3+}, Sm^{3+}, Nd^{3+})

Figure 3.13 (A) and (B) shows XRD patterns of $Sr_2P_2O_7$: 1.0 mol% Ce^{3+}, 1.0 mol% RE (RE = Eu^{3+}, Tb^{3+}, Dy^{3+}, Er^{3+} Gd^{3+}, Sm^{3+}, Nd^{3+}) and magnified XRD pattern for the 2θ range 25° - 35° to observe peak shifting occur due to the effect of various doping ion. The XRD patterns of rare earth co-doped $Sr_2P_2O_7$ samples are also compared with JCPDS standard card no. 24-1011. As rare earth doped $Sr_2P_2O_7$, rare earth co-doped $Sr_2P_2O_7$ have a single-phase. The structural parameters of the samples were analyzed using powderX software for XRD analysis which can confirms that the samples have a pure α-phase with crystallization in the orthorhombic structure and space group of Pnam. There is no significant change in XRD patterns of $Sr_2P_2O_7$ by changing the different RE^{3+} ions co-doped with Ce^{3+} as a fixed doping ion. This results into the single phase material where Sr^{2+} site is substituted by both RE^{3+} ions. The doping ions does not cause any substantial modification in the crystal structure of host. Figure 3.14 shows W-H plot of $Sr_2P_2O_7$: 1.0 mol% Ce^{3+}, 1.0 mol% RE (RE = Eu^{3+}, Tb^{3+}, Dy^{3+}, Er^{3+} Gd^{3+}, Sm^{3+}, Nd^{3+}). The average crystallite size of rare earth doped $Sr_2P_2O_7$ phosphors were calculated by the Scherrer's formula and W-H plot calculation method as mention in above section. Crystalline parameters and crystallite size of rare earth co-doped $Sr_2P_2O_7$ phosphors are summarized in Table 3.11.

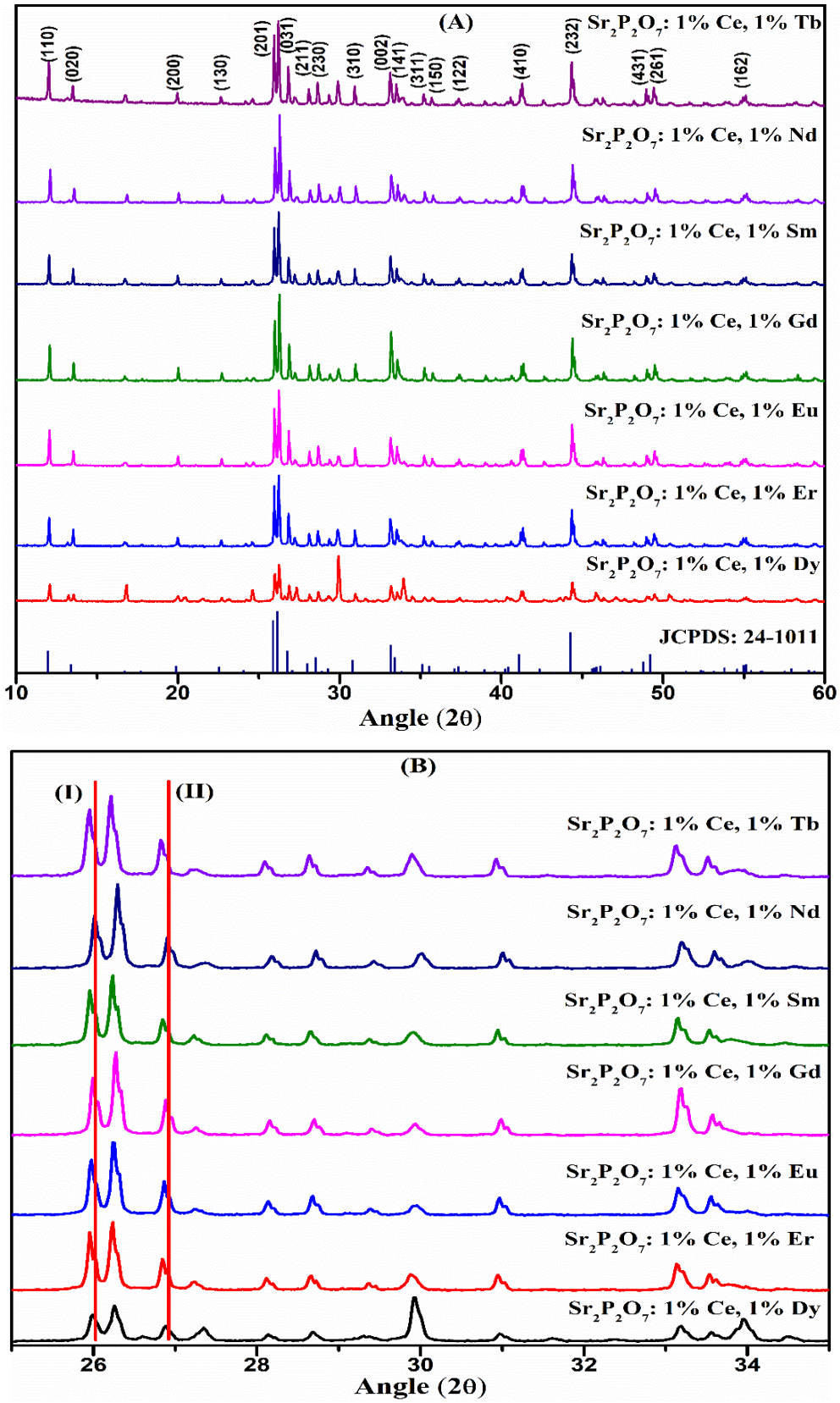

Figure 3.13 (A) XRD patterns of $Sr_2P_2O_7$: 1.0 mol% Ce^{3+}, 1.0 mol% RE (RE = Eu^{3+}, Tb^{3+}, Dy^{3+}, Er^{3+} Gd^{3+}, Sm^{3+}, Nd^{3+}) phosphor and JCPDs Card No. 24-1011; (B) Magnified XRD patterns.

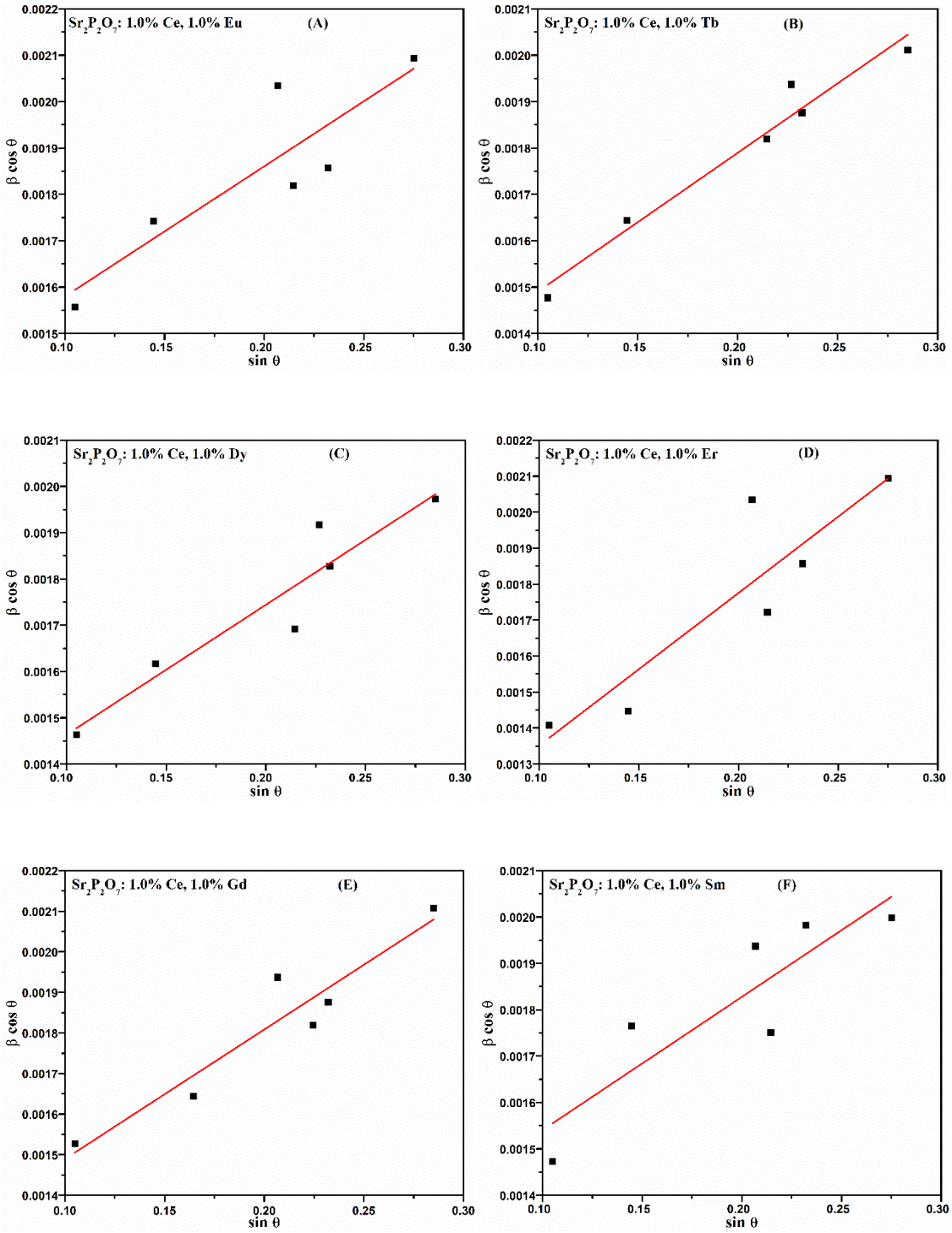

Figure 3.14 Williamson-Hall plot: (A) $Sr_2P_2O_7$: 1.0% Ce^{3+}, 1.0% Eu^{3+}; (B) $Sr_2P_2O_7$: 1.0% Ce^{3+}, 1.0% Tb^{3+}; (C) $Sr_2P_2O_7$: 1.0% Ce^{3+}, 1.0% Dy^{3+}; (D) $Sr_2P_2O_7$: 1.0% Ce^{3+}, 1.0% Er^{3+}; (E) $Sr_2P_2O_7$: 1.0% Ce^{3+}, 1.0% Gd^{3+}; (E) $Sr_2P_2O_7$: 1.0% Ce^{3+}, 1.0% Sm^{3+}phosphor.

Sample	Lattice Parameter			Volume of Unit Cell 'V' (Å ^{3})	Crystalline Size (nm)	
	a (Å)	b (Å)	c (Å)		Scherrer's formula	W-H Plot
$Sr_2P_2O_7$: Ce, Eu	8.872	13.177	5.431	634.92	76.39	80.45
$Sr_2P_2O_7$: Ce, Tb	8.858	13.161	5.415	631.28	72.24	73.89
$Sr_2P_2O_7$: Ce, Dy	8.838	13.142	5.409	638.25	71.46	73.12
$Sr_2P_2O_7$: Ce, Er	8.795	13.119	5.375	620.17	67.59	70.67
$Sr_2P_2O_7$: Ce, Gd	8.865	13.168	5.425	633.28	74.74	76.34
$Sr_2P_2O_7$: Ce, Sm	8.879	13.182	5.449	637.77	77.52	79.97
$Sr_2P_2O_7$: Ce, Nd	8.889	13.193	5.460	640.31	79.11	84.85

Table 3.11 Crystal structure parameters of $Sr_2P_2O_7$: 1.0 mol% Ce^{3+}, 1.0 mol% RE (RE = Eu^{3+}, Tb^{3+}, Dy^{3+}, Er^{3+} Gd^{3+}, Sm^{3+}, Nd^{3+}).

3.2.2. Fourier Transform Infrared Spectroscopy

3.2.2.1. $Sr_2P_2O_7$: RE (RE = Ce^{3+}, Eu^{3+}, Tb^{3+}, Dy^{3+}, Er^{3+}, Gd^{3+})

FTIR transmittance spectra of synthesized $Sr_2P_2O_7$: x RE (x = 0.5, 1.0, 1.5, 2.0, 2.5 and 5.0 mol%; RE = Ce^{3+}, Eu^{3+}, Tb^{3+}, Dy^{3+}, Er^{3+}, Gd^{3+}) were shown in Figure 3.15 – 3.20. The FTIR spectra of phosphors were recorded for the wavenumber range from 400 – 4000 cm^{-1}, the fingerprint region of the FTIR spectra of the range 400–2000 cm^{-1} has been demonstrated in the graph. All FTIR spectra were recorded from the KBr pellet of $Sr_2P_2O_7$. The KBr pellet for all samples were prepared for 99:1% ratio of KBr to $Sr_2P_2O_7$. The thickness of each pellet is approximately maintained up to 1 mm which has semi-transparent nature. Various transmittance bands of pyrophosphate group and phosphate group are observed in the FTIR spectra. FTIR spectra of the phosphors show the evidence of the multiple vibrational bands. The pyrophosphate group $(P_2O_7)^{4-}$ could be the form of O_3P-O-PO_3, and can be attributed to an assembly of the vibration modes of the PO_3 groups and the P-O-P groups [22]. The formation of the $P_2O_7^{4-}$ modes in the phosphor is conceded on the basis of the PO_3 and P-O-P vibrations. The phosphor prepared for different concentrations of doping ion, exhibit sharp bands in the region of wavenumber 1200–400 cm^{-1}. The FTIR spectra of $Sr_2P_2O_7$: x RE (x = 0.5, 1.0, 1.5, 2.0, 2.5 and 5.0 mol%; RE = Ce^{3+}, Eu^{3+}, Tb^{3+}, Dy^{3+}, Er^{3+}, Gd^{3+}) were consistent for all samples and there is no change in peak position as shown in Figure 3.15 – 3.20. The FTIR spectra of $Sr_2P_2O_7$ show characteristic bands at 433.90, 486.94, 500.43, 563.11,

620, 746.31, 974.84, 1014.37, 1047.16, 1062.58 and 1190.83 cm^{-1}. The intense peak attributed to the P-O-P symmetric stretching vibration mode is been observed at 746.31 and 974.84 cm^{-1} in the IR spectrum [44, 45]. It could be assigned to the symmetric stretching of the P-O-P bonds in the $(P_2O_7)^{4-}$ group. In the IR spectra of $Sr_2P_2O_7$, the peaks observed at 433.90, 486.94 and 500.43 cm^{-1} could be attributed to the δ-PO_3 deformation and ρ-PO_3 rocking modes [46-48]. The bands analogous to ν_{as} PO_3 mode with symmetric stretching attributed at 1190.83 and 1062.58 cm^{-1} in the infrared spectrum [49, 50]. The FTIR spectra have peaks positioned at 563.11 and 620 cm^{-1} are assigned corresponding to the asymmetric bending vibration ν_4 PO_4^{3-} groups [51]. The peaks positioned at 1014.37, 1047.16 and 1062.58 cm^{-1} attributed correspond to the asymmetric stretching mode of the ν_3 PO_4^{3-} groups [52]. The FTIR bands are manifest characteristic of the vibration modes of the pyrophosphate and phosphate groups in the phosphors. Thus, from the FTIR results it is found that the formation of phosphors were consistent and having uniform crystal phase formation as analyzed in x-ray diffraction.

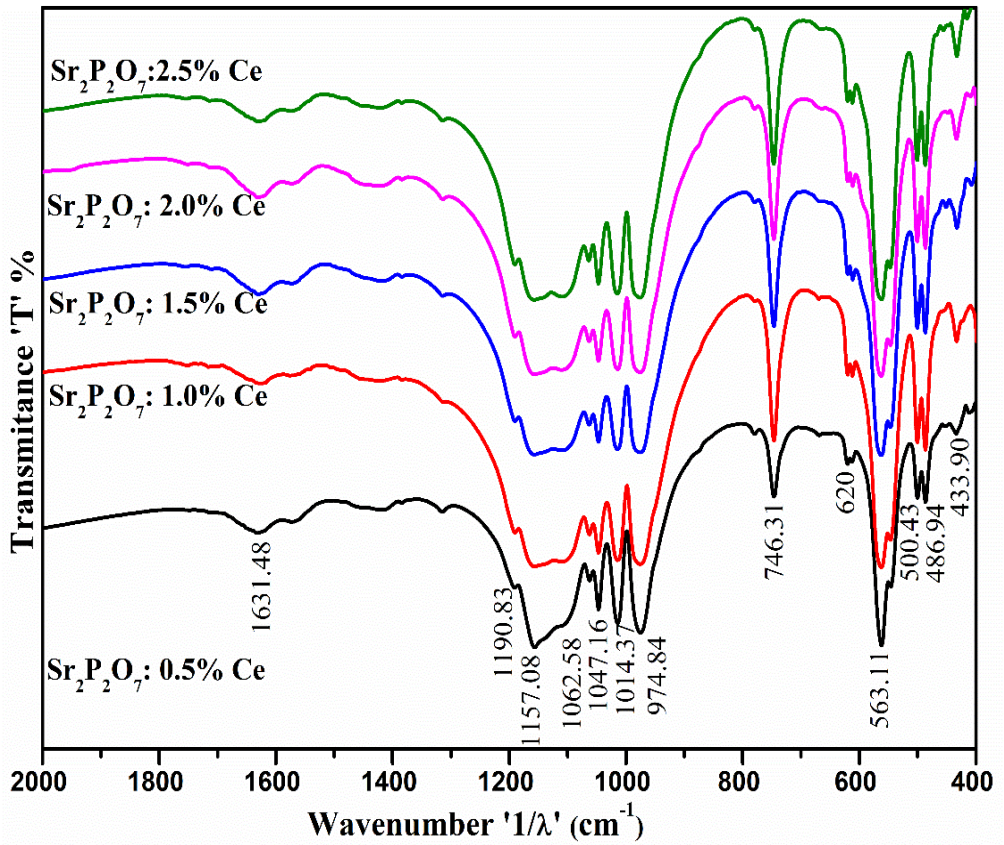

Figure 3.15 FTIR spectra of $Sr_2P_2O_7$: x Ce^{3+} (x = 0.5, 1.0, 1.5, 2.0 and 2.5 mol%).

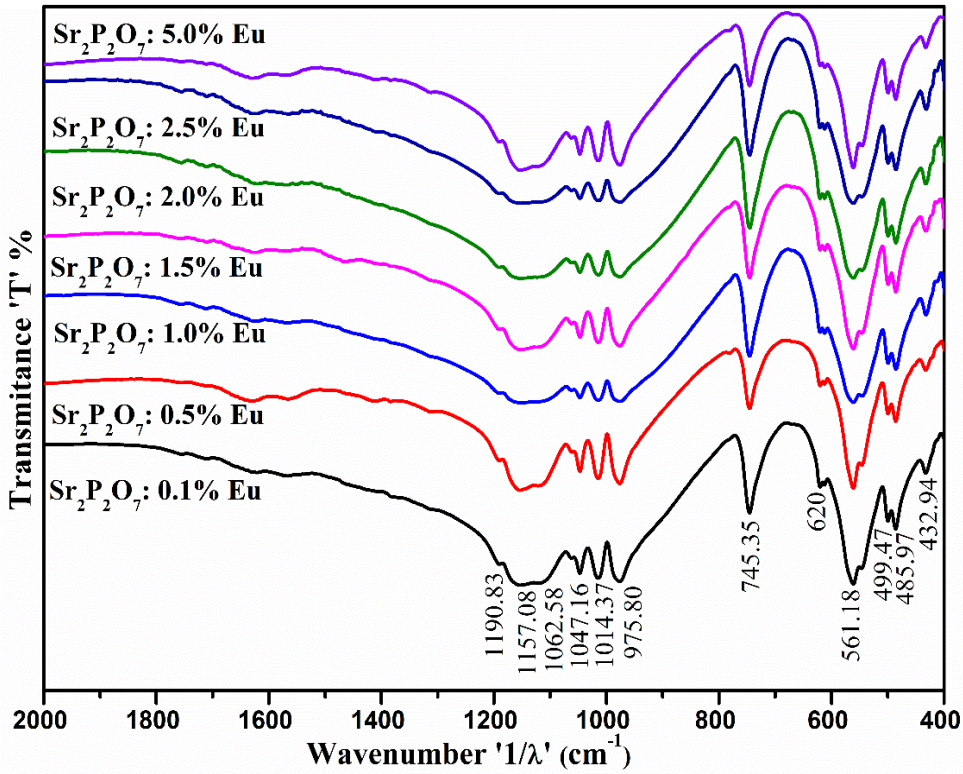

Figure 3.16 FTIR spectra of $Sr_2P_2O_7$: x Eu^{3+} (x = 0.1, 0.5, 1.0, 1.5, 2.0, 2.5 and 5.0 mol%).

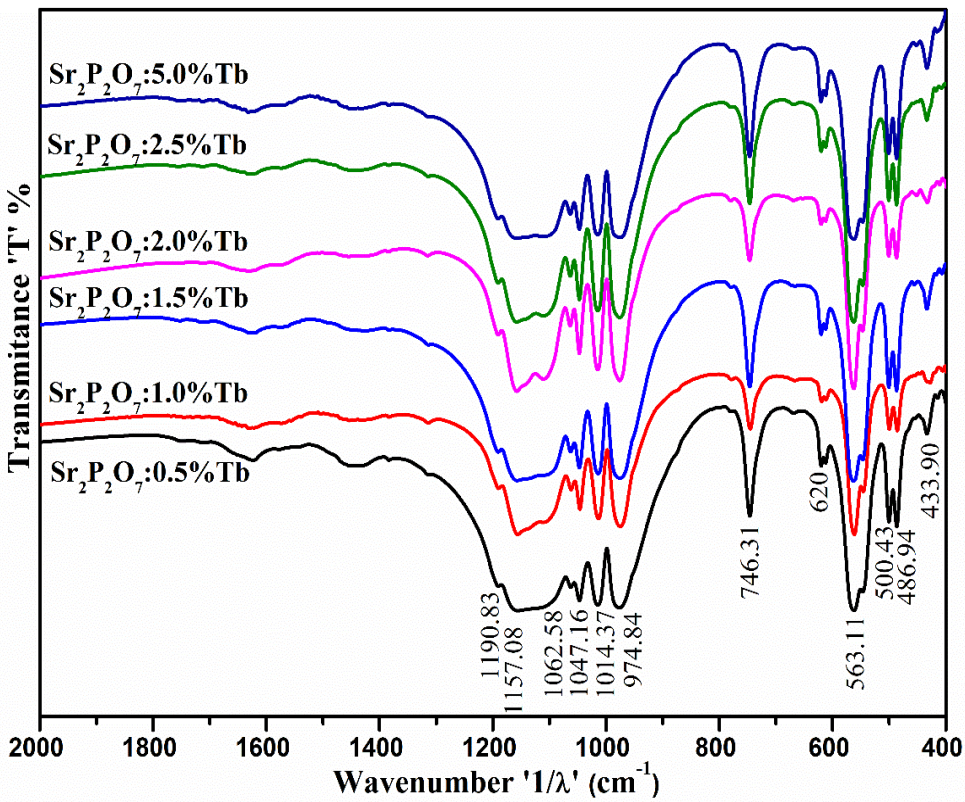

Figure 3.17 FTIR spectra of $Sr_2P_2O_7$: x Tb^{3+} (x = 0.5, 1.0, 1.5, 2.0, 2.5 and 5.0 mol%).

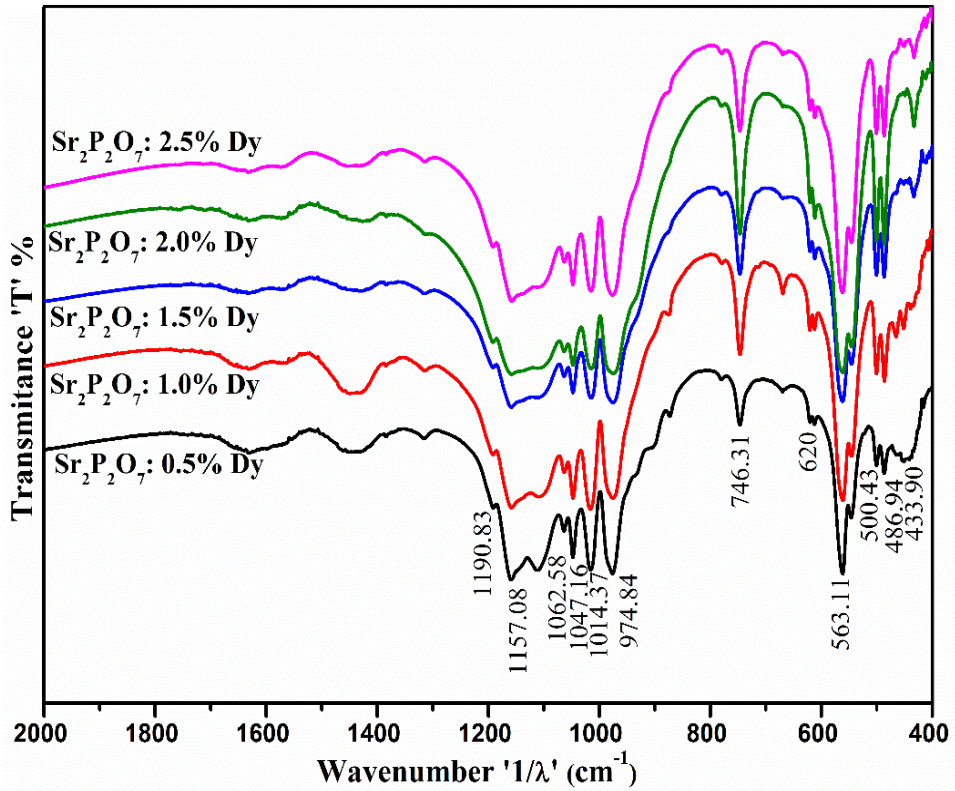

Figure 3.18 FTIR spectra of $Sr_2P_2O_7$: x Dy^{3+} (x = 0.5, 1.0, 1.5, 2.0 and 2.5 mol%).

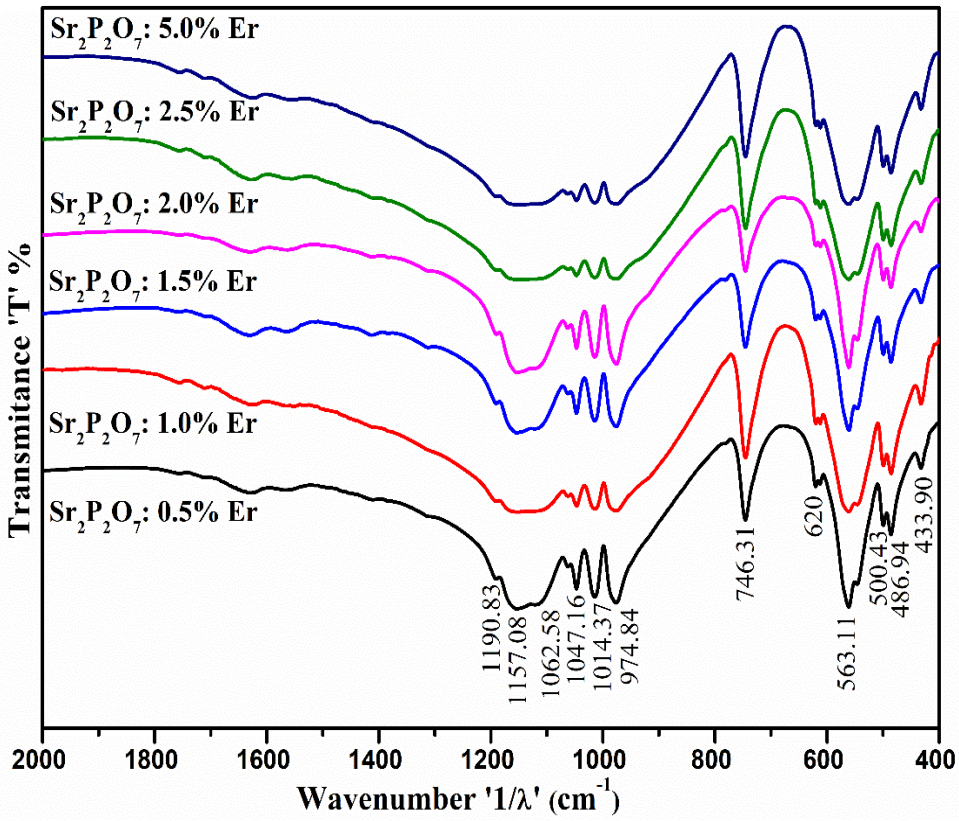

Figure 3.19 FTIR spectra of $Sr_2P_2O_7$: x Er^{3+} (x = 0.5, 1.0, 1.5, 2.0, 2.5 and 5.0 mol%).

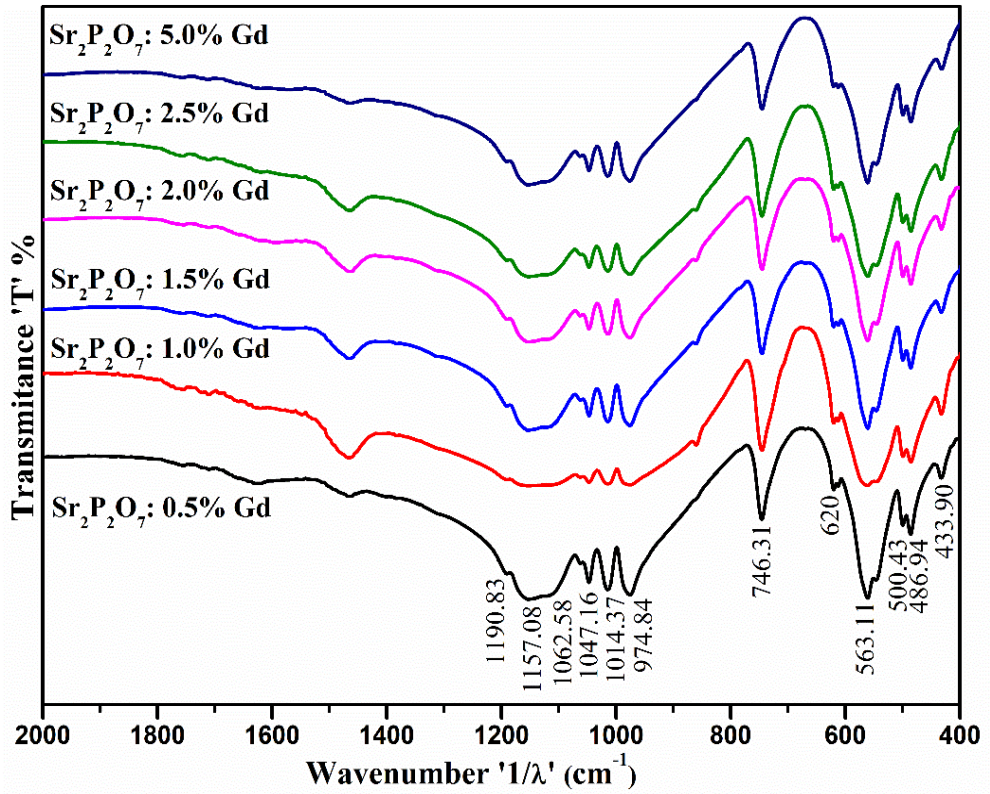

Figure 3.20 FTIR spectra of $Sr_2P_2O_7$: x Gd^{3+} (x = 0.5, 1.0, 1.5, 2.0, 2.5 and 5.0 mol%).

3.2.2.2. $Sr_2P_2O_7$: Ce^{3+}, RE (RE = Eu^{3+}, Tb^{3+}, Dy^{3+}, Er^{3+}, Gd^{3+}, Sm^{3+})

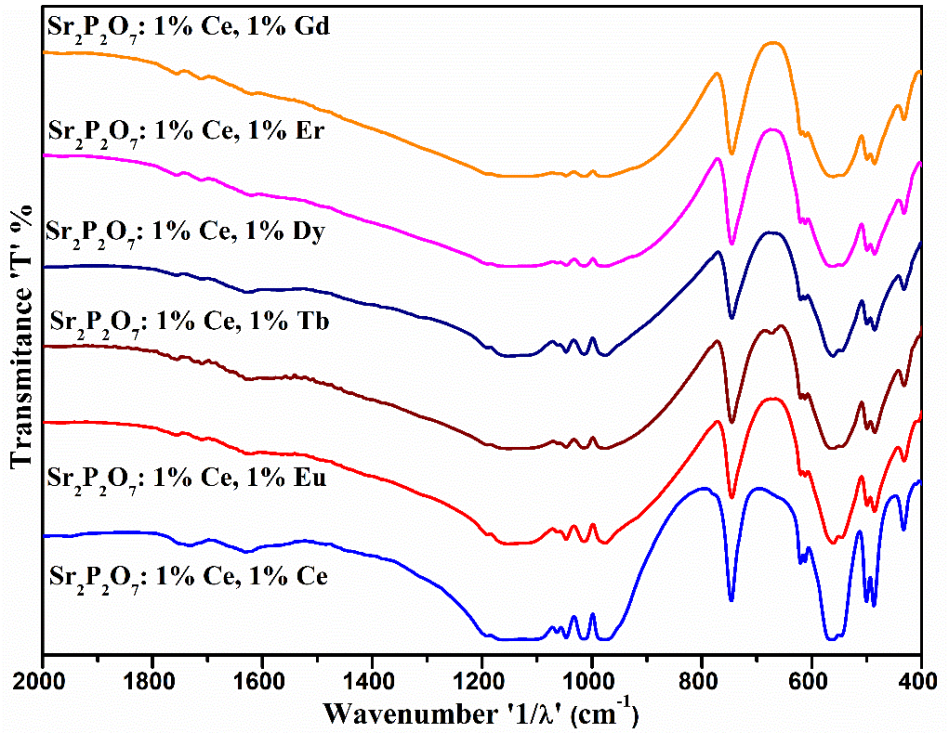

Figure 3.21 FTIR Spectra of $Sr_2P_2O_7$: 1.0 mol% Ce^{3+}, 1.0 mol% RE (RE = Eu^{3+}, Tb^{3+}, Dy^{3+}, Er^{3+} Gd^{3+} and Sm^{3+}).

Figure 3.21 shows the FTIR Spectra of $Sr_2P_2O_7$: 1.0mol% Ce^{3+}, 1.0 mol% RE (RE = Eu^{3+}, Tb^{3+}, Dy^{3+}, Er^{3+} Gd^{3+} and Sm^{3+}). The result shows that there is no significant variation occur in FTIR spectra of all rare earth co-doped $Sr_2P_2O_7$. The position of functional group band position remains unchanged as RE^{3+} doped $Sr_2P_2O_7$. FTIR results of all samples shows significant result as XRD. From the FTIR result that there is single phase formation of host $Sr_2P_2O_7$.

3.2.3. SEM

3.2.3.1. $Sr_2P_2O_7$: Ce^{3+}

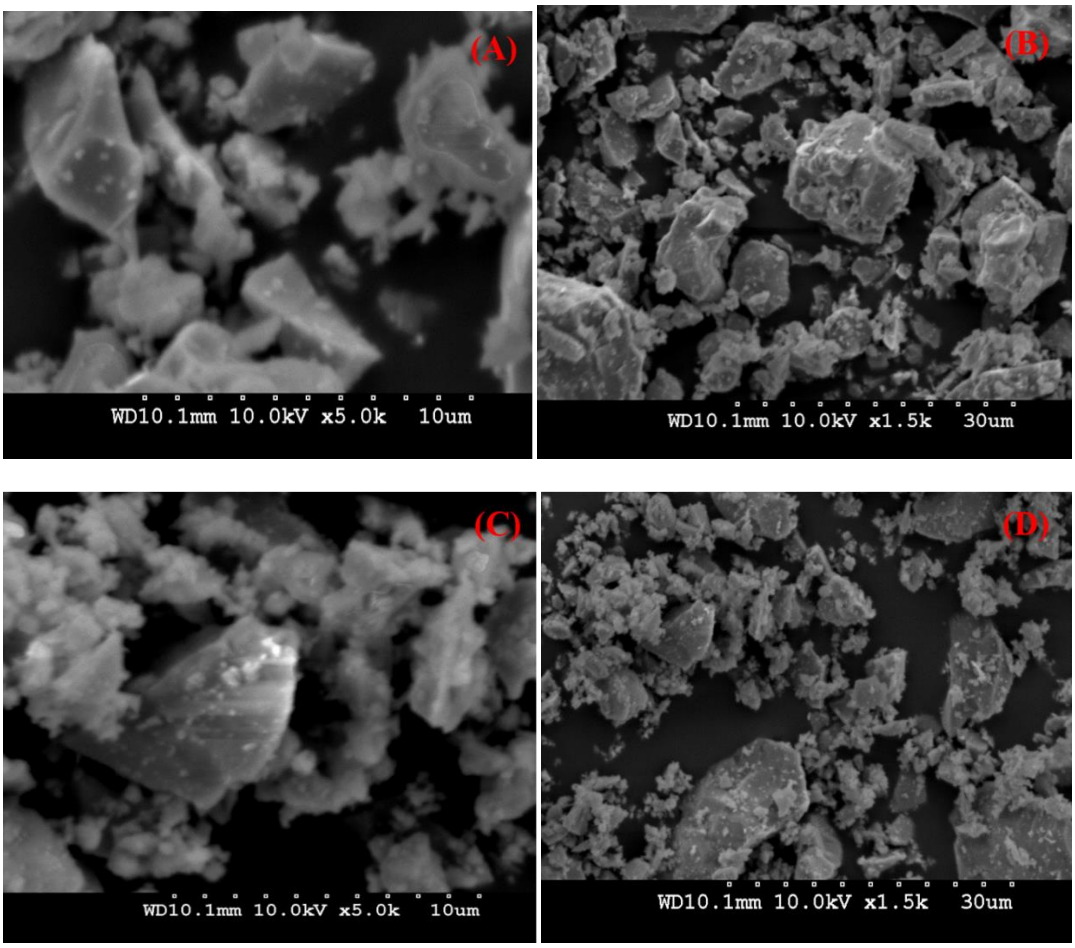

Figure 3.22 SEM images; (A), (B) $Sr_2P_2O_7$: 0.5 mol% Ce^{3+}; (C), (D) $Sr_2P_2O_7$: 2.0 mol% Ce^{3+}.

Figure 3.22 (A), (B) shows the SEM images of $Sr_2P_2O_7$: 0.5 mol% Ce^{3+} and Figure 3.22 (C), (D) shows the SEM images of $Sr_2P_2O_7$: 2.0 mol% Ce^{3+}. As shown in figure, all the phosphors are loosely agglomerated and are composed of particle of small size of the order of 2-5 µm in size. The material having complex stone like structure containing amassed particles. It is observed that the addition of Ce^{3+} does not

affect the shape and size of the samples with concentration variation. It is indicating that doping of rare earth ions does not induce any change in the morphology.

3.2.3.2. $Sr_2P_2O_7$: Eu^{3+}

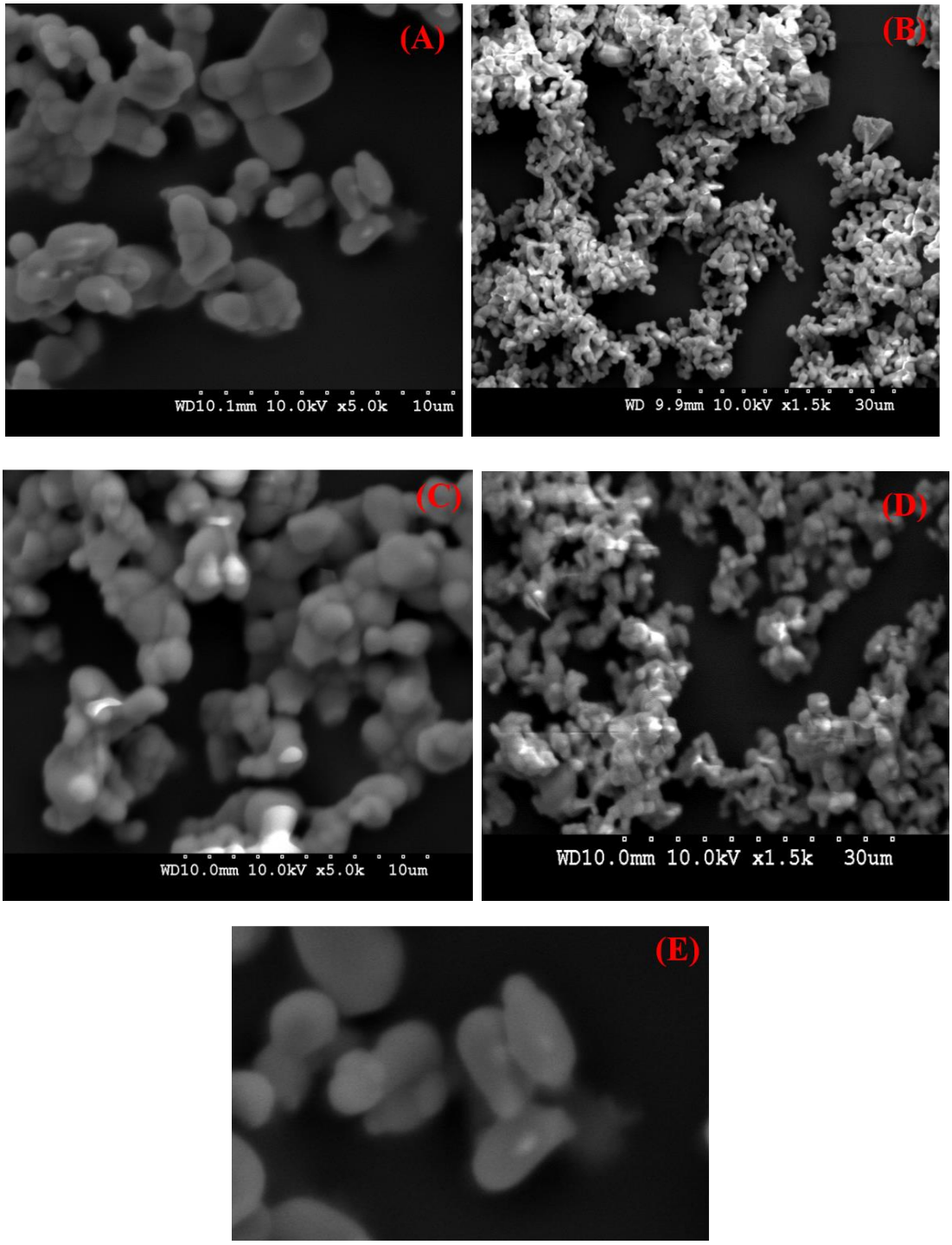

Figure 3.23 SEM images; (A), (B) Sr_2P_{27}: 1.0 mol% Eu^{3+}; (C), (D) $Sr_2P_2O_7$: 2.5 mol% Eu^{3+}.

The particle size and surface of the phosphors is significantly more important criterion for the commercial applications of the phosphors in solid state lighting. The phosphors having micron particles size and smooth surface can be feed well the commercial demand for WLEDs and lamp phosphors. Figure 3.23 (A), (B) shows the SEM images of $Sr_2P_2O_7$: 0.5 mol% Eu^{3+} and Figure 3.23 (C), (D) shows SEM images of $Sr_2P_2O_7$: 2.0 mol% Eu^{3+} synthesized at 1200 °C annealing temperatures. Figure 3.23 (E) shows the part unagglomerate particles in Figure 3.23 (A) of $Sr_2P_2O_7$: 2.0% Eu^{3+}, which could be appear like the shape of a capsule. The powder form of Eu^{3+} doped $Sr_2P_2O_7$ materializes in highly crystalline form with uneven morphology observed under different resolution and the average grain size of 2 – 3 μm. It is observed that the crystallites particles having nonuniform shape with evolved boundary of submicron size and strongly agglomerated. It could be occur due to the non-uniform temperature distribution during the firing of material by flux during synthesis. The surface morphology of the particles is smooth for both concentrations of doping which could be observed due to melting occurred at the surfaces of certain particles at high temperature.

3.2.3.3. $Sr_2P_2O_7$: Tb^{3+}

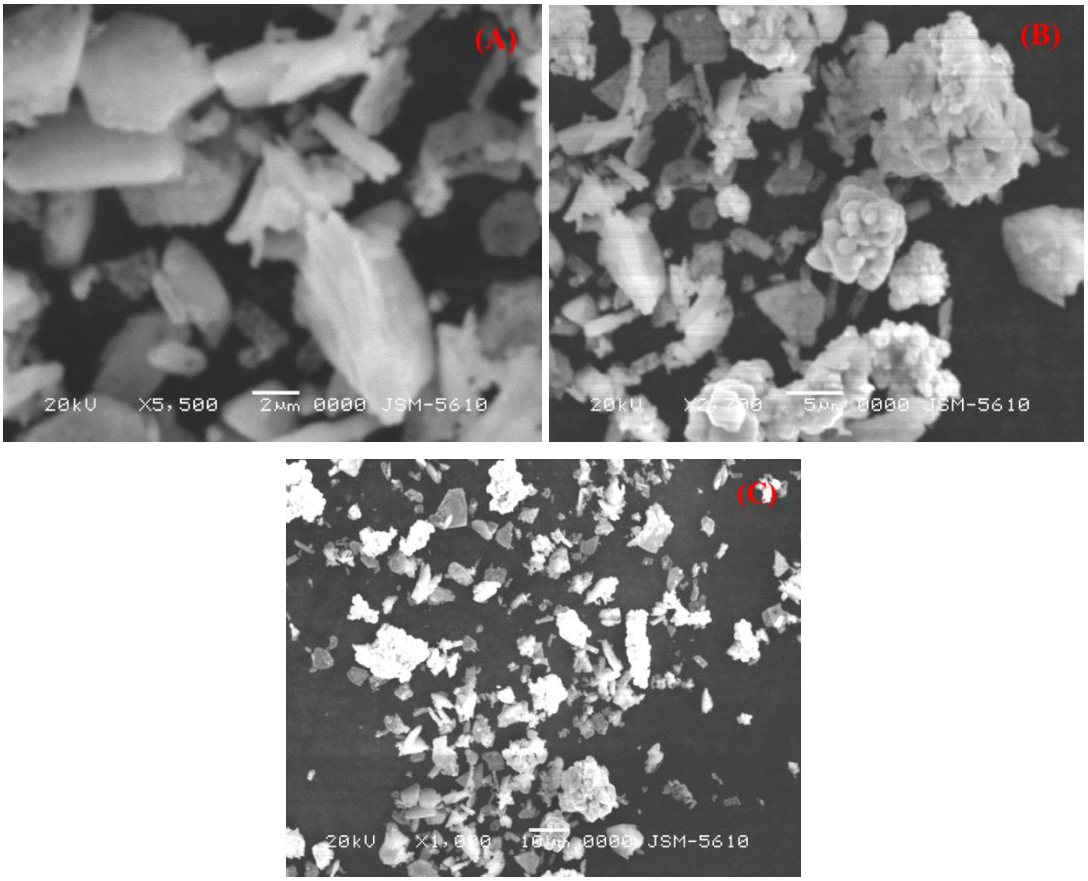

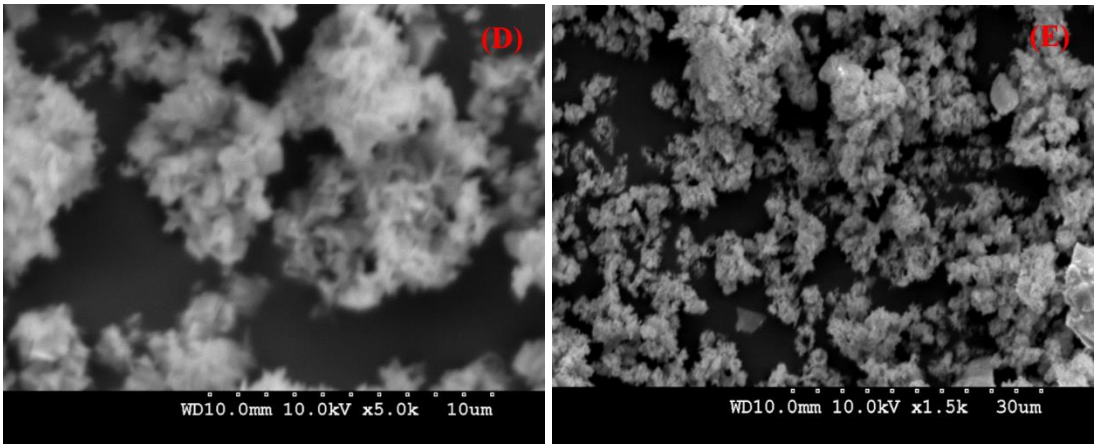

Figure 3.24 SEM images; (A), (B), (C) $Sr_2P_2O_7$: 0.5 mol% Tb^{3+}; (D), (E) $Sr_2P_2O_7$: 2.5 mol% Tb^{3+}.

SEM images representing the morphology of the synthesized sample are shown in Figure 3.24 (A), (B), (C) $Sr_2P_2O_7$: 0.5 mol% Tb^{3+}; (D), (E) $Sr_2P_2O_7$: 2.5 mol% Tb^{3+}. The images revealed that the phosphor have very porous structure of particles and it has possess foamy nature or cotton-like structure due to the highly agglomerated particles. An average particle size of the phosphors is of the range from 2 – 5 μm as seen in SEM images. In SEM, the particles of the phosphors are connected to each other that can give any conclusive information about the shape of the constituent particles.

References

1. Hammond, C., *The Basics of Crystallography and Diffraction*. Vol. 214. 2001: Oxford.
2. Beckhoff, B., et al., *Handbook of practical X-ray fluorescence analysis*, 2007: Springer Science & Business Media.
3. Connolly, J.R., *Elementary crystallography for X-ray diffraction.* EPS400-002, 2012.
4. Giannini, C., et al., *X-ray diffraction: a powerful technique for the multiple-length-scale structural analysis of nanomaterials.* Crystals, 2016. **6**(8): p. 87.
5. Sharma, R., et al., *X-ray diffraction: a powerful method of characterizing nanomaterials.* Recent research in science and technology, 2012. **4**(8).
6. Cullity, B.D. and S.R. Stock, *Elements of X-ray Diffraction*, 2014: Pearson Education.

7. Bunaciu, A.A., E.G. UdriŞTioiu, and H.Y. Aboul-Enein, *X-ray diffraction: instrumentation and applications.* Critical reviews in analytical chemistry, 2015. **45**(4): p. 289-299.
8. Bindu, P. and S. Thomas, *Estimation of lattice strain in ZnO nanoparticles: X-ray peak profile analysis.* Journal of Theoretical and Applied Physics, 2014. **8**(4): p. 123-134.
9. Creighton, T.E., *Proteins: structures and molecular properties*, 1993: Macmillan.
10. Fultz, B. and J.M. Howe, *Diffraction and the X-ray powder diffractometer*, in *Transmission Electron Microscopy and Diffractometry of Materials*, 2001, Springer. p. 1-61.
11. Klug, H.P. and L.E. Alexander, *X-ray diffraction procedures: for polycrystalline and amorphous materials.* X-Ray Diffraction Procedures: For Polycrystalline and Amorphous Materials, 2nd Edition, by Harold P. Klug, Leroy E. Alexander, pp. 992. ISBN 0-471-49369-4. Wiley-VCH, May 1974., 1974: p. 992.
12. Segneanu, A.E., et al., *Organic compounds FT-IR spectroscopy*, in *Macro To Nano Spectroscopy*, 2012, InTech.
13. Coates, J., *Interpretation of infrared spectra, a practical approach.* Encyclopedia of analytical chemistry, 2000. **12**: p. 10815-10837.
14. Stuart, B., *Infrared spectroscopy.* Kirk-Othmer Encyclopedia of Chemical Technology, 2005.
15. Theophanides, T., *Infrared spectroscopy-materials science, engineering and technology.* 2012.
16. Hsu, C.-P.S., *Infrared spectroscopy.* Handbook of instrumental techniques for analytical chemistry, 1997. **247**: p. 277.
17. Szczesniak, M., et al., *Effect of intermolecular interactions on the infrared spectrum of 1-methyluracil.* Spectrochimica Acta Part A: Molecular Spectroscopy, 1985. **41**(1-2): p. 237-250.
18. Valeur, B. and M.N. Berberan-Santos, *Molecular fluorescence: principles and applications*, 2012: John Wiley & Sons.
19. Moore, C.B., *A spectroscopist's view of energy states, energy transfers, and chemical reactions.* Annu. Rev. Phys. Chem., 2007. **58**: p. 1-33.

20. Schrader, B., *Infrared and Raman spectroscopy: methods and applications,* 2008: John Wiley & Sons.
21. Larkin, P., *Infrared and Raman spectroscopy: principles and spectral interpretation,* 2017: Elsevier.
22. Nakamoto, K., *Infrared and R aman Spectra of Inorganic and Coordination Compounds.* Handbook of Vibrational Spectroscopy, 2006.
23. Weyer, L. and J. Workman Jr, *Practical guide to interpretive near-infrared spectroscopy,* 2007: CRC press.
24. Siebert, F. and P. Hildebrandt, *Theory of infrared absorption and Raman spectroscopy.* Vibrational Spectroscopy in Life Science, 2008: p. 11-16.
25. Griffiths, P.R. and J.A. De Haseth, *Fourier transform infrared spectrometry*. Vol. 171. 2007: John Wiley & Sons.
26. Faix, O., *Fourier transform infrared spectroscopy*, in *Methods in lignin chemistry,* 1992, Springer. p. 83-109.
27. Theophanides, T., *Introduction to infrared spectroscopy*, in *Infrared Spectroscopy-Materials Science, Engineering and Technology,* 2012, InTech.
28. Humphreys, J., R. Beanland, and P.J. Goodhew, *Electron microscopy and analysis,* 2014: CRC Press.
29. Egerton, R.F., *Physical principles of electron microscopy,* 2005: Springer.
30. Reimer, L., *Scanning electron microscopy: physics of image formation and microanalysis*. Vol. 45. 2013: Springer.
31. Goldstein, J.I., et al., *Scanning electron microscopy and X-ray microanalysis,* 2017: Springer.
32. Lloyd, G.E., *Atomic number and crystallographic contrast images with the SEM: a review of backscattered electron techniques.* Mineralogical Magazine, 1987. **51**(359): p. 3-19.
33. Bogner, A., et al., *A history of scanning electron microscopy developments: towards "wet-STEM" imaging.* Micron, 2007. **38**(4): p. 390-401.
34. Barbier, J. and J.P. Echard, *A New Refinement of* α-$Sr_2P_2O_7$. Acta Crystallographica Section C, 1998. **54**(12): p. IUC9800070-IUC9800070.
35. Monshi, A., M.R. Foroughi, and M.R. Monshi, *Modified Scherrer equation to estimate more accurately nano-crystallite size using XRD.* World Journal of Nano Science and Engineering, 2012. **2**(3): p. 154-160.

36. Irfan, H., M. Racik K, and S. Anand, *Microstructural evaluation of $CoAl_2O_4$ nanoparticles by Williamson–Hall and size–strain plot methods.* Journal of Asian Ceramic Societies, 2018. **6**(1): p. 54-62.
37. Shannon, R.D., *Revised effective ionic radii and systematic studies of interatomic distances in halides and chalcogenides.* Acta crystallographica Section A: crystal physics, diffraction, theoretical and general crystallography, 1976. **32**(5): p. 751-767.
38. D'Angelo, P., et al., *Revised ionic radii of lanthanoid (III) ions in aqueous solution.* Inorganic chemistry, 2011. **50**(10): p. 4572-4579.
39. Bispo, A.G., et al., *Red phosphor based on Eu^{3+}-isoelectronically doped Ba_2SiO_4 obtained via sol-gel route for solid-state lighting.* RSC Advances, 2017. **7**(85): p. 53752-53762.
40. Pires, A.M. and M.R. Davolos, *Luminescence of europium (III) and manganese (II) in barium and zinc orthosilicate.* Chemistry of materials, 2001. **13**(1): p. 21-27.
41. Hou, D., et al., *Luminescence of Ce^{3+} at two different sites in α-$Sr_2P_2O_7$ under vacuum ultraviolet-UV and x-ray excitation.* Journal of Applied Physics, 2010. **108**(8): p. 083527.
42. Han, B., et al., *The effect of Li^+ ions on the luminescent properties of a single-phase white light-emitting phosphor α-$Sr_2P_2O_7$: Dy^{3+}.* Dalton Transactions, 2015. **44**(17): p. 7854-7861.
43. Zhou, R., et al., *Photoluminescence characteristics of Sm^{3+} doped $Sr_2P_2O_7$ as new orange-red emitting phosphor.* Journal of Alloys and Compounds, 2015. **647**: p. 136-140.
44. Boonchom, B. and R. Baitahe, *Synthesis and characterization of nanocrystalline manganese pyrophosphate Mn2P2O7.* Materials Letters, 2009. **63**(26): p. 2218-2220.
45. Sun, L., et al., *Preparation and properties of nanoparticles of calcium phosphates with various Ca/P ratios.* Journal of research of the National Institute of Standards and Technology, 2010. **115**(4): p. 243.
46. Paques-Ledent, M.-T., *Vibrational spectra and structure of $LiB^{2+}PO_4$ compounds with B= Sr, Ba, Pb.* Journal of Solid State Chemistry, 1978. **23**(1-2): p. 147-154.

47. Pillai, V.M., et al., *Infrared and Raman spectra of $Cs_2VOP_2O_7$ and single crystal $Rb_2(VO)_3(P_2O_7)_2$.* Spectrochimica Acta Part A: Molecular and Biomolecular Spectroscopy, 1999. **55**(9): p. 1809-1817.

48. Vincent, V., et al., *Infrared spectroscopy and X-ray diffraction studies of the $Ca_2P_2O_7/Na_4P_2O_7$ system.* European journal of solid state and inorganic chemistry, 1997. **34**(6): p. 571-587.

49. Khay, N., A. Ennaciri, and M. Harcharras, *Vibrational spectra of double diphosphates $RbLnP_2O_7$ (Ln= Dy, Ho, Y, Er, Tm, Yb).* Vibrational Spectroscopy, 2001. **27**(2): p. 119-126.

50. Velchuri, R., et al., *Solid-State Syntheses of Rare-Earth-Doped $Sr_{1-x}Ln_{2x/3}MgP_2O_7$ (Ln= Gd, Eu, Dy, Sm, Pr, and Nd; x= 0.05) by Metathesis Reactions and their Spectroscopic Characterization.* Spectroscopy Letters, 2011. **44**(4): p. 258-266.

51. Vasant, S.R. and M. Joshi, *Synthesis and characterization of nanoparticles of calcium pyrophosphate.* Modern Physics Letters B, 2011. **25**(01): p. 53-62.

52. Frost, R.L., et al., *A vibrational spectroscopic study of the phosphate mineral whiteite $CaMn^{++}Mg_2Al_2(PO_4)_4(OH)_2{\cdot}8(H_2O)$.* Spectrochimica Acta Part A: Molecular and Biomolecular Spectroscopy, 2014. **124**: p. 243-248.